Received: 28 June 2019 | Revised: 23 July 2019 | Accepted: 1 August 2019

DOI: 10.1002/inf2.12042

REVIEW ARTICLE

WILEY

Challenges and perspectives for manganese-based oxides for advanced aqueous zinc-ion batteries

Yinlei Zhao[1,2†] | **Yunhai Zhu**[1,3†] | **Xinbo Zhang**[1,2]

[1]State Key Laboratory of Rare Earth Resource Utilization, Changchun Institute of Applied Chemistry, Chinese Academy of Sciences, Changchun, China

[2]University of Science and Technology of China (USTC), Hefei, China

[3]Key Laboratory of Automobile Materials (Jilin University), Ministry of Education, Department of Materials Science and Engineering, Jilin University, Changchun, China

Correspondence
Xinbo Zhang, State Key Laboratory of Rare Earth Resource Utilization, Changchun Institute of Applied Chemistry, Chinese Academy of Sciences, Changchun, China.
Email: xbzhang@ciac.ac.cn

Funding information
People's Government of Jilin Province; National Natural Science Foundation of China

Abstract

Li-ion batteries (LIBs) with excellent cycling stability and high-energy densities have already occupied the commercial rechargeable battery market. Unfortunately, the high cost and intrinsic insecurity induced by organic electrolyte severely hinder their applications in large-scale energy storage. In contrast, aqueous Zn-ion batteries (ZIBs) are being developed as an ideal candidate because of their cheapness and high security. Benefiting from high operating voltage and acceptable specific capacity, recently, manganese-based oxides with different various crystal structures have been extensively studied as cathode materials for aqueous ZIBs. This review presents research progress of manganese-based cathodes in aqueous ZIBs, including various manganese-based oxides and their zinc storage mechanisms. In addition, we also discuss some optimization strategies that aim at improving the electrochemical performance of manganese-based cathodes, and the design of flexible aqueous ZIBs based on manganese-based cathodes (MZIBs). Finally, this review summarizes some valuable research directions, which will promote the further development of aqueous MZIBs.

KEYWORDS

flexible ZIBs, manganese dioxide, manganese-based oxides, strategies, ZIBs

1 | INTRODUCTION

With the increasing energy requirements and the environmental deterioration caused by the using of traditional fossil fuels, it is the trend of the times to develop clean and renewable energy for a sustainable energy supply. However, the existing sustainable energy (eg, solar, wind, and water) is intermittent, requiring effective mediums to store and transfer energy when the sustainable energy is unavailable.[1-12] Among various energy storage technologies, rechargeable batteries are believed to be the most feasible choice for large-scale energy storage system because of their long cycle life, high energy efficiency, and simple maintenance.[13-19]

To date, diverse rechargeable batteries with different charge carriers (such as Li^+, Na^+, K^+, Ca^{2+}, Mg^{2+}, Zn^{2+}, and Al^{3+}) have been successfully demonstrated in organic or aqueous systems.[20-41] Generally, owing to the wider electrochemical window of organic electrolyte, nonaqueous batteries always exhibit higher energy density than the aqueous one. Unfortunately, the use of organic electrolytes may cause serious safety and environmental risks due to their toxic, flammable, and volatile nature.[10,42-44] Unlike nonaqueous batteries, aqueous batteries employ water solution as the electrolyte, owning favorable advantages, including cheapness, high security, and environmentally friendly.

[†]These authors contributed equally to this study.

Besides, the aqueous electrolytes have much higher ionic conductivity than organic electrolytes, significantly improving the rate and rapid charge performance of batteries. These unique natures of aqueous batteries make them ideally suitable for large-scale energy system.[45-52]

Recently, aqueous zinc-ion batteries (ZIBs) have been attracting tremendous interest as the most favorable candidate, since the Zn anode possesses low redox potential, high theoretical capacity, and excellent stability in water.[53-58] Additionally, divalent zinc ions transfer two electrons, allowing ZIBs to achieve high capacity and an acceptable energy density. Different from the traditional LIBs in a rocking-chair fashion, the zinc storage mechanisms in aqueous ZIBs system are intricate and debatable. Currently, there are three main reaction mechanisms in the aqueous ZIBs: Zn^{2+} insertion/extraction,[36,59,60] chemical conversion reaction,[61,62] and H^+/Zn^{2+} insertion/extraction,[63,64] as schematically demonstrated in Figure 1. Notably, during the chemical conversion reaction, the cathode reversibly change in composition and structure, accompanied by dissolution/deposition of $Zn_xSO_4(OH)_{2x+2}{\cdot}yH_2O$ on its surface (Figure 1C, D). Up to now, reversible Zn-ion storage in various host materials has been identified, such as manganese-based oxides, vanadium-based materials,[37,63,65-67] and Prussian blue analogs.[68-71] Among them, manganese-based electrode materials with low cost, abundant resource, and pronounced structural stability, exhibit high specific capacity and operating voltage, rendering them most promising for Zn-ion storage.

In this review, we will summarize the structural characteristics and energy storage mechanism of different manganese-based oxides in aqueous ZIBs. Subsequently, some strategies are discussed for performance optimization of manganese-based cathodes, involving construction of nanostructures, compositing with conductive substrates, introduction of defects, adjustment of interlayer spacing, and optimization of electrolytes. Furthermore, this review discusses the design of flexible ZIBs based on manganese-based cathode materials (MZIBs). Finally, this review gives unique insights into the valuable research directions of aqueous MZIBs. And we believe that this review of future prospects and research directions will promote the further development of aqueous MZIBs.

2 | MANGANESE-BASED OXIDES

Due to the advantages of cheapness, rich source, environmental protection, and nonpoisonous, manganese (Mn)-

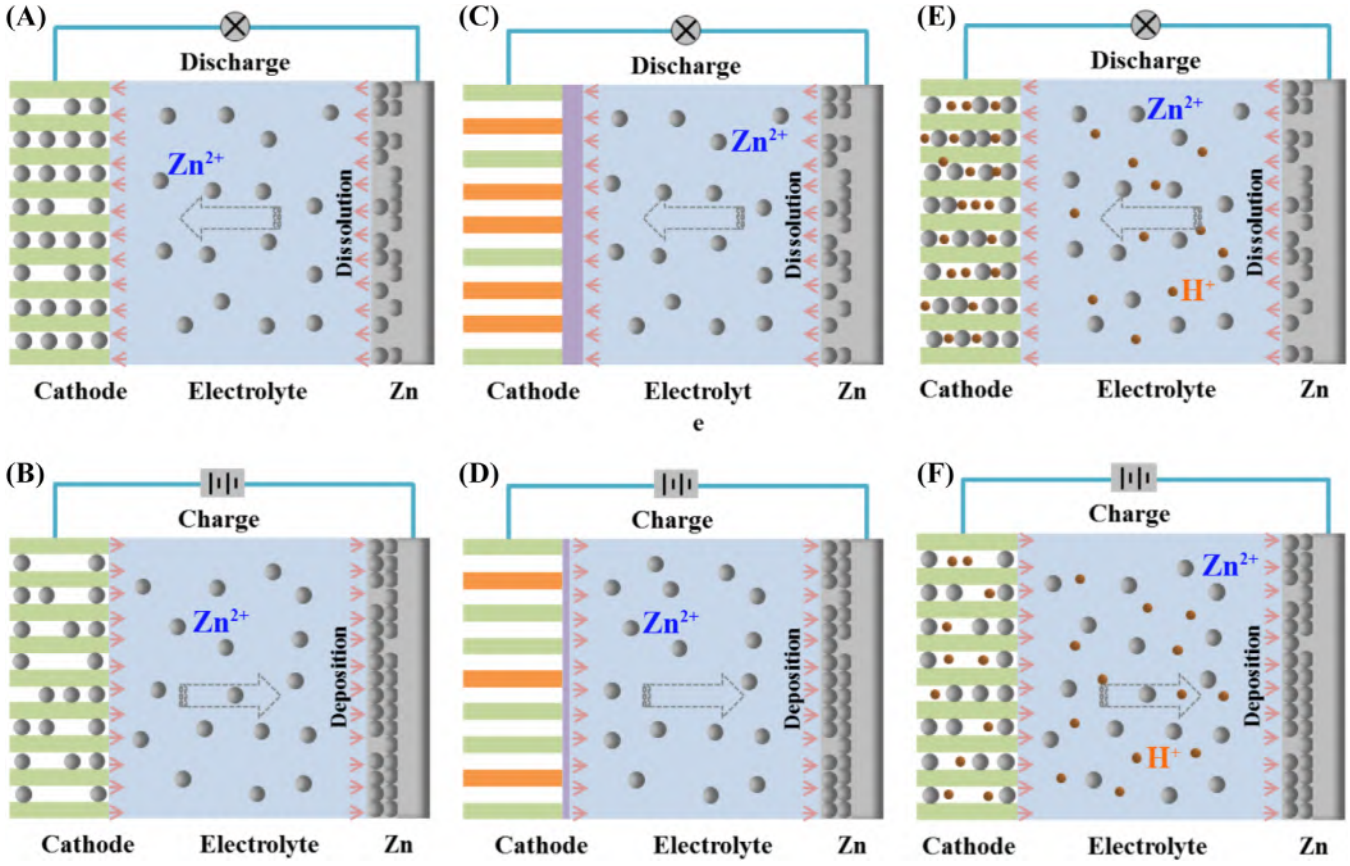

FIGURE 1 Schematics of the chemistry of the zinc-ion battery based on different reaction mechanisms. A,B, Zn^{2+} insertion/extraction. C,D, Chemical conversion reaction. E,F, H^+/Zn^{2+} insertion/extraction

based oxides with various valence states (Mn^{2+}, Mn^{3+}, Mn^{4+} and Mn^{7+}), are supported to be very promising energy storage materials. Lately, manganese-based oxides, such as manganese dioxide (MnO_2) with diverse crystal structures, Mn_2O_3, Mn_2O_4, Mn_3O_4, are developed as one of the most favorable cathode materials for aqueous ZIBs.

2.1 | Manganese dioxide

It is well-known that MnO_2 exists in various crystal forms such as α-MnO_2, β-MnO_2, ε-MnO_2, γ-MnO_2, δ-MnO_2, and todorokite-type MnO_2. In these structures, the basic structural unit MnO_6 octahedra is connected to each other by co-angle/co-edge, constructing chain, tunnel, layered structures with enough space accommodating foreign cations.[72-75] Given this structural advantage, MnO_2 has been extensively investigated as favorable cathodes for batteries in the past several years, including Li-ion batteries,[76,77] Na-ion batteries,[78] K-ion batteries,[79] Mg-ion batteries,[80-82] and latest ZIB.[83-86] Theoretically, MnO_2 can accommodate one Zn^{2+} insertion per formula with a high theoretical capacity of approximately 616 mAh/g, in which the Mn^{4+} is reduced to Mn^{2+}. To date, numerous MZIBs have been reported with satisfactory electrochemical performances and regarded as very promising candidates for large-scale energy storage.[53-57]

2.1.1 | β-MnO_2

β-MnO_2 possesses a [1 × 1] tunnel (2.3 × 2.3 Å) structure. And the *c*-axis of β-MnO_2 consists of single chains of [MnO_6] octahedral units by sharing corners (Figure 4A). Some studies have successfully proved that β-MnO_2 has excellent zinc storage performance.[86-89] A previous study by Kang et al[90] revealed that massive β-MnO_2 delivered low electrochemical activity in ZIBs. In a subsequent work, Kang et al[91] achieved reversible insertion/extraction of Zn^{2+} ions into/from β-MnO_2 with a porous framework. Unfortunately, Zn-insertion mechanism was not discussed. Later, Kim et al[61] successfully synthesized β-MnO_2 nanorod via a rapid microwave-assisted hydrothermal reaction, which delivered a discharge capacity as high as 270 mAh/g (Figure 2D). Here, the zinc ions storage in β-MnO_2 nanorod electrode had been proved to be performed via both solid solution and conversion reactions. During these reactions, Zn^{2+} goes into the β-MnO_2 framework. And the Zn-inserted phases form and $ZnSO_4$•$3Zn(OH)_2$•$5H_2O$ precipitates on the electrode surface. The local structural change of the β-MnO_2 nanorod electrode during Zn^{2+} insertion/extraction was further clarified with x-ray absorption near edge structure (Figure 2C). These studies indicated that structure of β-MnO_2 nanorod is well-preserved during the insertion/extraction of Zn^{2+} ions, being consistent with the x-ray diffraction (XRD) results (Figure 2B). Recently, Chen et al[62] reported a high-performance rechargeable aqueous Zn-MnO_2 battery with β-MnO_2 cathode, achieving a high capacity of 225 mAh/g. In their studies, β-MnO_2 with tunnel structure is shown to undergo a phase transition process to layered zinc-buserite during the first discharge process followed by reversible Zn^{2+} (de)intercalation from/into $Zn_{0.5}Mn^{3+}O_2{\cdot}5H_2O$ (Figure 2E). The XRD (Figure 2F) results confirmed this Zn^{2+} insertion mechanism and structural transformation of MnO_2 cathode again.

2.1.2 | γ-MnO_2

The low temperature γ-MnO_2 phase is composed of stochastically distributed 1 × 1 (2.3 × 2.3 Å) and 1 × 2 (2.3 × 4.6 Å) tunnel blocks,[92,93] showing excellent zinc storage performance. The ZIBs with γ-MnO_2 as the cathode were assembled for the first time by Yamamoto et al,[94] realizing the rechargeable Zn-MnO_2 battery. Subsequently, Kumar et al[95] reported reversible insertion/extraction of zinc ions in Zn/γ-MnO_2 battery with a gel polymer electrolyte based on polyvinylidene fluoride and zinc triflate. To our regret, the Zn^{2+} insertion/extraction mechanism in γ-MnO_2 was not clarified in these above studies. In this aspect, Kim et al[96] has filled in the void. As shown in Figure 3, with the continuous embedding of Zn^{2+} ions, γ-MnO_2 will eventually form layered-type γ-$Zn_yMn^{2+}O_4$ after phase transformation. In the process, interestingly, there will be the appearance of intermediate phases such as a spinel $ZnMn_2{}^{3+}O_4$ and tunnel-type γ-$Zn_xMn^{2+}O_4$, which will not disappear completely. More importantly, all phases are almost completely restored to the γ-MnO_2 phase in subsequent fully charged state. Furthermore, the researchers also found that most of these phases with multioxidation states could revert back to the parent γ-MnO_2 phase during the battery cycling.

2.1.3 | α-MnO_2

As the most commonly studied MnO_2, the α-MnO_2 has one-dimensional 2 × 2 tunnels (4.6 × 4.6 Å) in its crystal structure, enabling efficient storage and fast diffusion for foreign cations along the *z*-axis (Figure 2A).[97] Since the first demonstration of Zn-ion activity for α-MnO_2 in neutral zinc sulfate electrolyte by Kang et al in 2009,[98] several attempts have been made to study the electrochemical properties of α-MnO_2 in aqueous ZIBs. For instance, in a study of Kang et al,[90] the α-MnO_2 cathode (Figure 4A) delivered a high capacity of 210 mAh/g. And it was revealed that Zn^{2+} could be embedded in α-MnO_2 to form

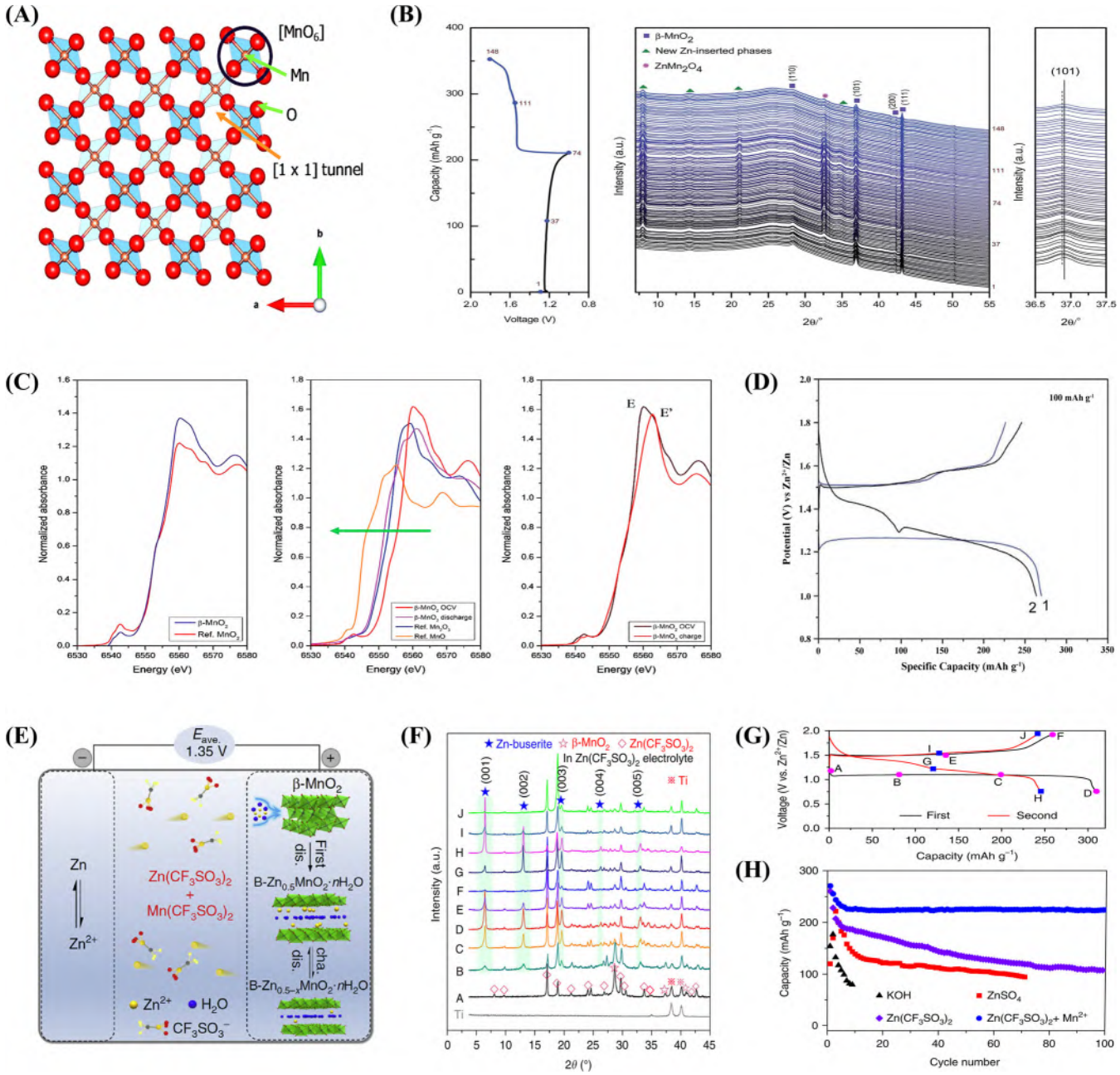

FIGURE 2 A, Crystallographic structure of the β-MnO_2. B, In situ synchrotron XRD pattern of the β-MnO_2 nanorod cathode recorded during electrochemical discharge/charge and a close up view of the corresponding (101) plane reflection. C, XANES spectra of β-MnO_2 powder and standard MnO_2 and Ex situ XANES spectra of the β-MnO_2 nanorod cathode collected after discharging/charging in the Zn test cell. D, Initial discharge/charge profiles of the β-MnO_2 nanorod cathode in the Zn test cell. Reproduced with permission from Ref. 61, Copyright 2017, American Chemical Society. E, The rechargeable Zn/β-MnO_2 cell. F, XRD patterns of a β-MnO_2 electrode at selected states during the first and second cycles. G, Typical charge/discharge curves for the initial two cycles at 0.32 C in 3 M $Zn(CF_3SO_3)_2$ aqueous electrolyte. The points A-J marked the states where data were collected for XRD analysis. H, Comparison of the cycling performance of Zn-MnO_2 cells with electrolytes of 45 wt% KOH (at 0.32 C), 3 M $ZnSO_4$, 3 M $Zn(CF_3SO_3)_2$, and 3 M $Zn(CF_3SO_3)_2$ with 0.1 M $Mn(CF_3SO_3)_2$ additive at 0.65 C. nC equals the rate to charge/discharge the theoretical capacity (308 mAh/g) of MnO_2 in 1/*n* hours. Reproduced with permission from Ref. 62, Copyright 2017, Nature Publishing Group

$ZnMn_2O_4$ phase during discharge process by XRD (Figure 4B). Upon charging process, reversal transformation occurs, demonstrating it is highly reversible (Figure 4C). Consequently, the embedding mechanism of Zn^{2+} in α-MnO_2 can be described by the following Equation (1):

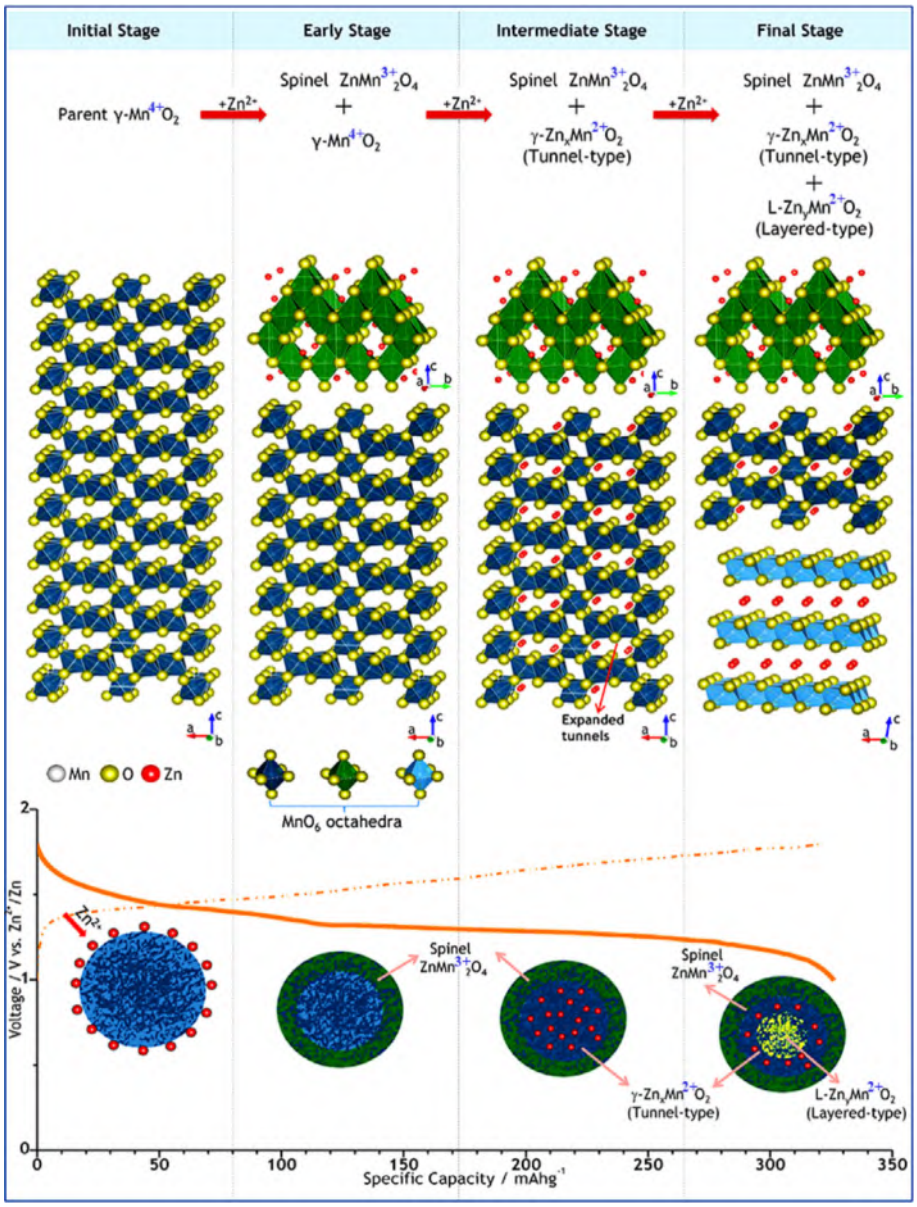

FIGURE 3 Schematic illustration of the reaction pathway of Zn-insertion in the prepared γ-MnO_2 cathode. Reproduced with permission from Ref. 96, Copyright 2014, ACS Publications

$$Zn^{2+} + 2e^- + 2\alpha - MnO_2 \leftrightarrow ZnMn_2O_4 \quad (1)$$

Subsequently, Kim et al[64] revealed the change in the valence state of manganese during charge and discharge process by XANES analysis. In detail, the tetravalent manganese is completely converted into trivalent in the discharge process (Figure 4D), while the trivalent manganese is completely converted to tetravalent during the charging process (Figure 4E). This demonstrated again that the zinc storage behavior of α-MnO_2 is reversible. Furthermore, the two distinct peaks are observed at 1.3 and 1.2 V in the CV curves (Figure 4F). Inspired by this, Kim et al speculated Zn^{2+} insertion into the a-MnO_2 cathode may be carried out in two steps, as follows:

$$0.5Zn^{2+} + 2\alpha - MnO_2 + e^- \leftrightarrow Zn_{0.5}Mn_2O_4 \quad (2)$$

$$0.5Zn^{2+} + Zn_{0.5}Mn_2O_4 + e^- \leftrightarrow ZnMn_2O_4 \quad (3)$$

However, sufficient evidence for this mechanism was not provided in this work and further exploration was needed. Recently, Oh et al[99] discovered a new mechanism that a reversible phase change takes place between α-MnO_2 and layered Zn-birnessite upon the Zn^{2+} ion insertion/extraction (Figure 4G). Specifically, nearly one-third of Mn in α-MnO_2

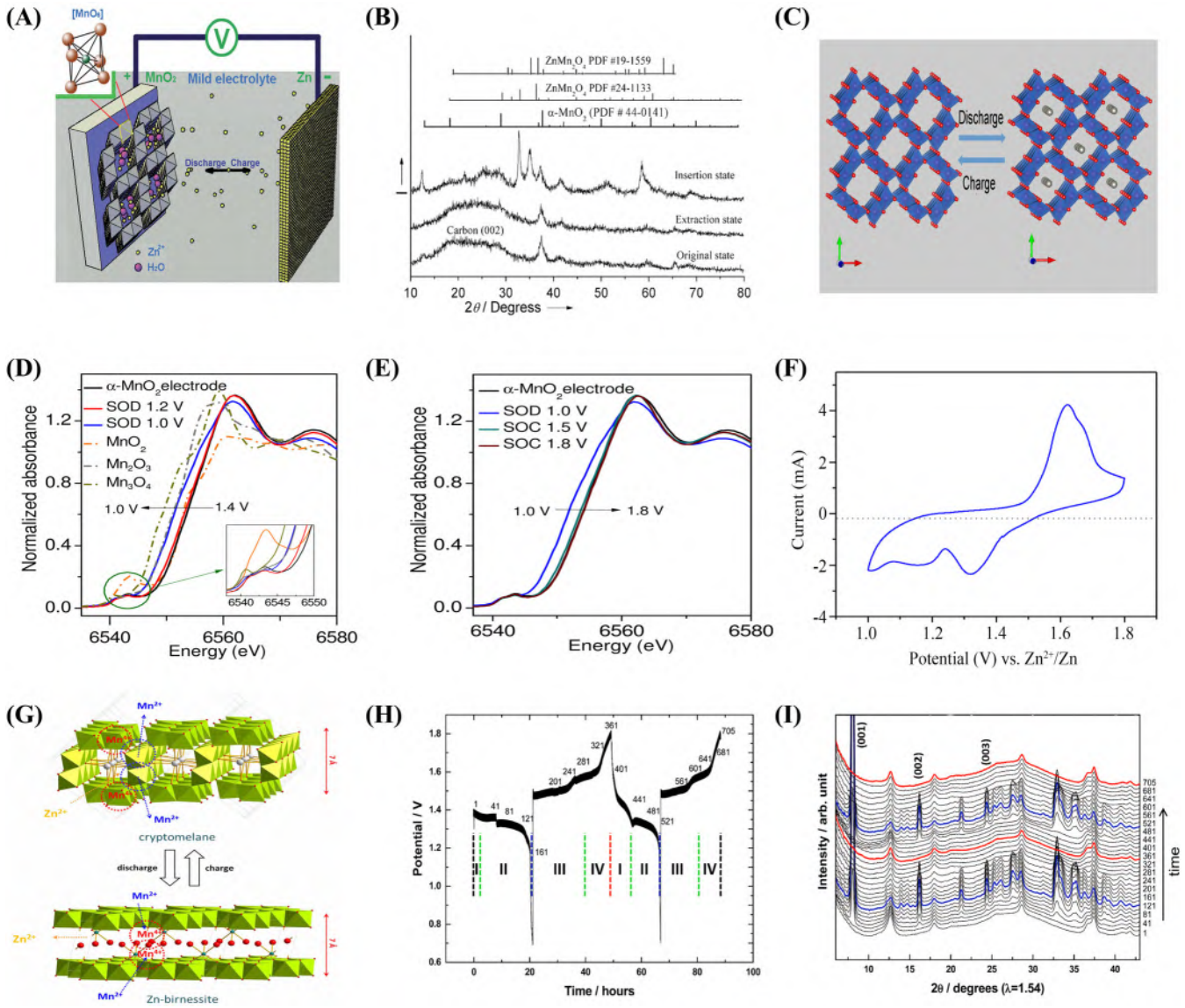

FIGURE 4 A, Schematics of the chemistry of the zinc-ion battery. Zn^{2+} ions migrate between tunnels of an α-MnO_2 cathode and a Zn anode. The inset in the upper left corner shows the structural basic unit of the MnO_6 octahedron of MnO_2. B, Zn 2p core level spectra of cathodic crystalline α-MnO_2 electrodes in the original, extraction, and insertion states. C, Schematic illustration of Zn^{2+} intercalation mechanism in α-MnO_2 cathode. Reproduced with permission from Ref. 90, Copyright 2012, Wiley-VCH. D, E, Ex-situ XANES of α-MnO_2 nanorods electrode recorded in various discharge/recharge states in zinc-ion cells. The XANES spectra of standard MnO_2, Mn_2O_3, and Mn_3O_4 are provided in, E, for comparison purposes. F, Cyclic voltammograms at a scan rate of 0.5 mV/s of α-MnO_2 nanorods electrode. Reproduced with permission from Ref. 64, Copyright 2015, Elsevier Ltd. G, Phase transition mechanism in α-MnO_2 during Zn^{2+} (de-)intercalation. Reproduced with permission from Ref. 99, Copyright 2014, Nature Publishing Group. H, The charge-discharge profile of the zinc/α-MnO_2 for the first two cycles at a scan rate of C/20 (1C = 210 mA/g of the active mass). I, The corresponding in situ XRD patterns during the electrochemical cycling. The regions of interest are described as I, II, III, and IV in, H. Reproduced with permission from Ref. 100, Copyright 2015, Royal Society of Chemistry

swims into the electrolyte, accompanied by the formation of Zn-birnessite (Equations (4) and (5)) during the discharge process. Upon charging, it is fully recovered to form the original a-MnO_2 structure (Equation (6)).

$$Mn^{4+}(s) + e^{-} \leftrightarrow Mn^{3+}(s) \quad (4)$$

$$Mn^{3+} \leftrightarrow Mn^{4+}(s) + Mn^{2+}(aq) \quad (5)$$

$$Mn^{2+}(aq) \leftrightarrow Mn^{4+}(s) + 2e^{-} \quad (6)$$

Later, Oh et al[100] proposed a different understanding for Zn^{2+} insertion into a-MnO_2. Unlike previous reports, here, it

was confirmed that the direct discharge product is layered Zn-buserite. And Zn-birnessite is produced after the buserite lose its Zn^{2+} ions and H_2O molecules. The XRD results show a single-phase region at the early stage of discharge (region I) and the end of charge (region IV), corresponding to sloping part of cyclic voltammograms (Figure 4H, I). Unfortunately, the reaction mechanism for the single-phase region remains unknown.

Apart from the above reaction mechanisms mentioned, a chemical conversion reaction mechanism based on reversible precipitation/dissolution of $Zn_4(OH)_6SO_4{\cdot}nH_2O$ (ZHS) has also been proposed (Figure 5A).[101] For the first time, Oh et al found that the ZHS is obtained after fully discharging, and disappears after fully charging (Figure 5B). Notably, only α-MnO_2 is observed in discharged electrode after washing with acetic acid (Figure 5B). These results indicated that ZHS forms on the electrode surface upon discharge process, and no Zn^{2+} ion or proton is embedded in the α-MnO_2. Simultaneously, the researchers found that the pH value of the electrolyte gradually increases during discharge. Besides, results of AAS show that the Mn^{2+} concentration in electrolyte increases with the depth of discharge while that of Zn^{2+} decreases with the depth of discharge. The researchers attributed these phenomena to the disproportionality of the unstable Mn^{3+}, which increases the pH of the electrolyte and induces subsequent precipitation process. The pathways of these reactions are listed below:

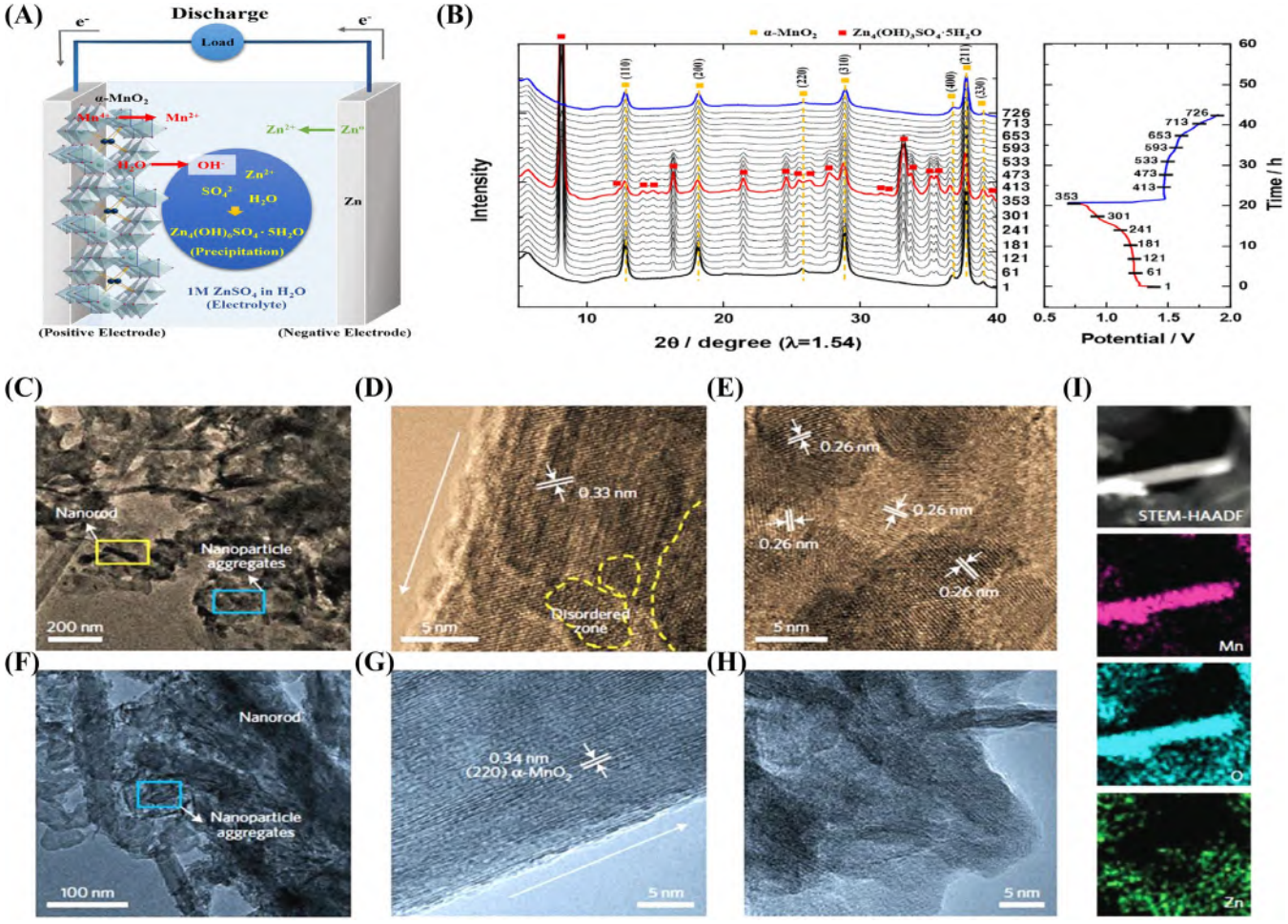

FIGURE 5 A, Schematic showing the reactions during the discharge process for a-MnO_2/Zn cell employing aqueous $ZnSO_4$ electrolyte. B, In situ XRD patterns of a cathode in a Zn/a-MnO_2 cell with 1.0 m $ZnSO_4$ aqueous electrolyte during the first discharge–charge cycle at a rate of C/20 and the corresponding discharge–charge curve. Reproduced with permission from Ref. 101, Copyright 2016, Wiley-VCH. C-H, TEM/high resolution TEM images of MnO_2 electrodes during electrochemical process. MnO_2 electrodes discharged to 1 V (C-E) and then charged back to 1.8 V in the first cycle (F-H). The yellow and blue rectangular regions have a morphology typical for short nanorods and nanoparticle aggregates, respectively. The arrows in d and g indicate the growth directions of the short nanorods. I, (STEM-high-angle annular dark field image of short nanorods and scanning transmission electron microscopy -energy disperse spectroscopy (STEM-EDS) mappings of the elemental distributions of Mn, O, and Zn in the MnO_2 electrode in the discharged state during the first cycle. Reproduced with permission from Ref. 102, Copyright 2016, Nature Publishing Group

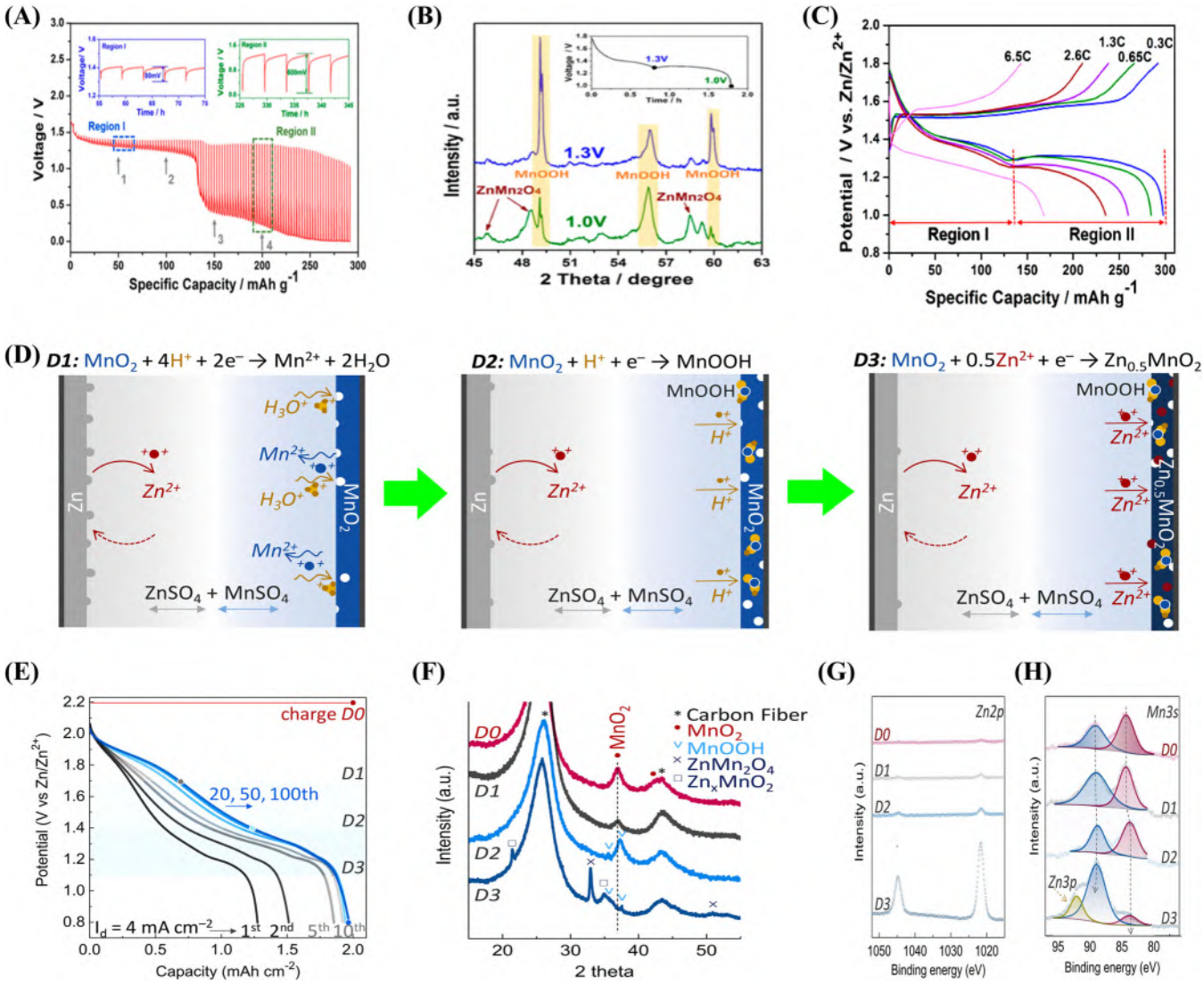

FIGURE 6 A, Discharge galvanostatic intermittent titration technique (GITT) profiles of the Zn/MnO_2@CFP cell (50 mA/g for 120 seconds followed by a 4 hours rest). B, Ex situ XRD patterns of the MnO_2@CFP cathode at depth of discharge at 1.3 and 1.0 V, respectively. C, Charge and discharge curves of the Zn/MnO_2@CFP cell in 2 M $ZnSO_4$ + 0.2 M $MnSO_4$ electrolyte at different rates in first cycle. Reproduced with permission from Ref. 110, Copyright 2017, ACS Publications. D, Schematic of galvanostatic discharge, including D1, D2, and D3 steps. E, Galvanostatic discharge curves in the first 100 cycles. Three shaded areas indicate three charge transfer steps in correspondence with D1, D2, and D3. F,G, Ex situ XRD and x-ray photoelectron spectroscopy (XPS) patterns of the MnO_2 cathode at various depth of discharge of D0 (full charge), D1 (1.7 V), D2 (1.4 V), and D3 (0.8 V) in initial discharge. High-resolution XPS of the Zn2p, G, and Mn3s, H. The hollow-circles correspond to the experimental spectra, and the blue and red curves represent fitted results of the spectra of Mn3s. The yellow curve is the fitted component of the Zn3p peak. Reproduced with permission from Ref. 111, Copyright 2019, Wiley-VCH

$$MnO_2 + + 2H_2O + 2e^- \leftrightarrow Mn^{2+} + 4OH^- \quad (9)$$

$$4Zn^{2+} + SO_4{}^{2-} + 6OH^- + 5H_2O \leftrightarrow Zn_4(OH)_6SO_4 \bullet 5H_2O \downarrow \quad (10)$$

For the formation mechanism of ZHS, another view, based on different reaction mechanisms on the cathode (a chemical conversion between α-MnO_2 and MnOOH), was proposed by Liu et al.[102] In this view, α-MnO_2 could react with H^+ from water to form MnOOH and OH^- ($H_2O \leftrightarrow H^+ + OH^-$, $MnO_2 + H^+ + e^- \leftrightarrow$ MnOOH). And then, ZHS forms on the electrode surface caused by the reaction of OH^-, $ZnSO_4$, and H_2O ($1/2\ Zn^{2+} + OH^- + 1/6\ ZnSO_4 + x/6\ H_2O \leftrightarrow 1/6\ ZnSO_4[Zn(OH)_2]_3 \bullet XH_2O$). Here, the formations of MnOOH and $ZnSO_4[Zn(OH)_2]_3 \cdot xH_2O$ are observed in the XRD patterns of α-MnO_2 electrode after discharge to 1 V in the first cycle. To further verify this, the changes of structure and morphology of the α-MnO_2 electrodes during cycling were investigated with transmission

electron microscope (TEM) and STEM-EDS. As shown in Figure 5D, E, the lattice spacing of discharge products is 0.33 and 0.26 nm, corresponding to the d spaces of (210) and (020) planes in monoclinic MnOOH. Furthermore, as shown in Figure 5I, the element of O and Mn distribute on the short nanorods and nanoparticles and Zn mainly distributes on the surface of flaky compounds, which indicate the formation of $ZnSO_4[Zn(OH)_2]_3{\cdot}xH_2O$ on the cathode surface (Figure 5I). In the charged state, the nanorods and polymerized nanoparticles still maintain their morphology, while the lattice distance and crystalline almost return to those of the pristine α-MnO_2 cathode. These results indicate that structural transformation of α-MnO_2 cathode during cycling is reversible. Lately, Liang et al[103] reported a new understanding for H^+-storage mechanism that the diffusion of H^+ into $K_{0.8}Mn_8O_{16}$ host results in simultaneous insertion ($H_xK_{0.8}Mn_8O_{16}$) and conversion (MnOOH or $K_{0.1}$MnOOH) reaction. Interestingly, the similar phenomena are also observed in the α-MnO_2 electrode. Here, the $K_{0.8}Mn_8O_{16}$ electrode delivered excellent electrochemical performance, such as considerable energy density and outstanding cyclic stability, which may be attributed to that the reaction kinetics of H^+ storage may be much faster than that of Zn^{2+} storage because of the much smaller size and lower valent state of H^+ than Zn^{2+}. At the same time, this is a good support for the mechanism proposed above.

2.1.4 | Todorokite-Type MnO_2

Todorokite-type MnO_2 with 3×3 tunnel (7.0×7.0 Å) structure is composed of four edges sharing MnO_6 octahedral panels. Cations and H_2O molecules could be embedded in its tunnels to form $M_{1 \pm x}Mn_6O_{12}{\cdot}3\text{-}4H_2O$ (M = Na, Ca, Mg, Ba, K etc.), which keep the structure stable.[103-107] For example, todorokite-type MnO_2 with embedded Mg^{2+} and water molecules ($Mg_{1.8}Mn_6O_{12}{\cdot}4.8H_2O$) was constructed as cathode in aqueous ZIBs.[108] Here, only a limited discharged capacity of 108 mAh/g was shown at 0.5 C. Interestingly, the todorokite-type MnO_2 exhibited good cycle and rate capability, benefiting from the large tunnel and electrostatic shielding between the zinc ions and the host structure caused by the structural water. Nevertheless, the mechanism of Zn^{2+} embedding in todookite remains unclear and more in-depth research is desired.

2.1.5 | ε-MnO_2

Akhtenskite-structure MnO_2 (ε-MnO_2) is a metastable phase composed of face-shared [MnO_6] and [YO_6] octahedral (Y means vacancy), where Mn^{4+} cations randomly occupy 50% of the octahedral positions of the hexagonal-close-packed (hcp) oxygen sublattice.[109] Wang et al[110] prepared the composite electrode of ε-MnO_2 nanoflakes and carbon fiber paper by in situ electrodeposition. And the discharge capacity of the composite electrode is 290 mAh/g (Figure 6C). Importantly, the co-intercalation mechanism of H^+ and Zn^{2+} was first proposed in rechargeable aqueous ZIBs by electrochemical and structural analysis. As shown in Figure 5C, with the rise of charge and discharge rate, the changes of voltage and capacity in the two regions indicate a large difference in kinetics. Moreover, the total overvoltage of the first region is much lower than the second region. However, the reaction equilibrium voltage of the second region is only slightly lower than the first region (Figure 6A). Theoretically, the progressive voltage change during discharge in the GITT test is caused by ion diffusion. Therefore, the authors speculated that the voltage platform of region I is most likely induced by H^+ insertion, while the voltage platform of region II is mainly attributed to Zn^{2+} insertion. Subsequently, this guess was supported by XRD. As shown in Figure 6B, MnOOH and $ZnMn_2O_4$ are observed when the battery were discharged to 1.3 and 1.0 V, respectively. Recently, Qiao et al[111] prepared a new high-voltage electrolytic Zn-MnO_2 battery by activating proton and electron kinetics, which maximized the electrolysis process (Figure 6D). Unlike other Zn-based batteries, this Zn-MnO_2 battery exhibited an amazing discharge voltage platform of 1.95 V and a high specific capacity of 570 mAh/g. More importantly, a new electrolysis mechanism was proposed by various means of characterization (Figure 6F-H). As is shown in Figure 6E, there are three discharge regions that is, D1 (2.0-1.7 V), D2 (1.7-1.4 V), and D3 (1.4-0.8 V) in the discharge profiles. Dissolution of MnO_2 occurs in the D1 region followed by H^+ insertion (D2) and Zn^{2+} insertion (D3) into MnO_2, which are highly reversible. The reaction mechanism can be summarized:

Anode:

$$Zn^{2+} + 2e^- \leftrightarrow Zn \text{ all cycles} \quad (11)$$

Cathode:

$$Mn^{2+} + 2H_2O \rightarrow MnO_2 + 4H^+ + 2e^- \text{ initial charge process} \quad (12)$$

$$MnO_2 + 4H^+ + 2e^- \leftrightarrow Mn^{2+} + 2H_2O \text{ flowing cycles} \quad (13)$$

$$MnO_2 + H^+ + e^- \leftrightarrow MnOOH \text{ flowing cycles} \quad (14)$$

$$MnO_2 + 0.5Zn^{2+} + e^- \leftrightarrow Zn_{0.5}MnO_2 \text{ flowing cycles} \quad (15)$$

This work has offered new insight into the advancement of MZIBs and can help to realize the practical application of low-cost energy storage device.

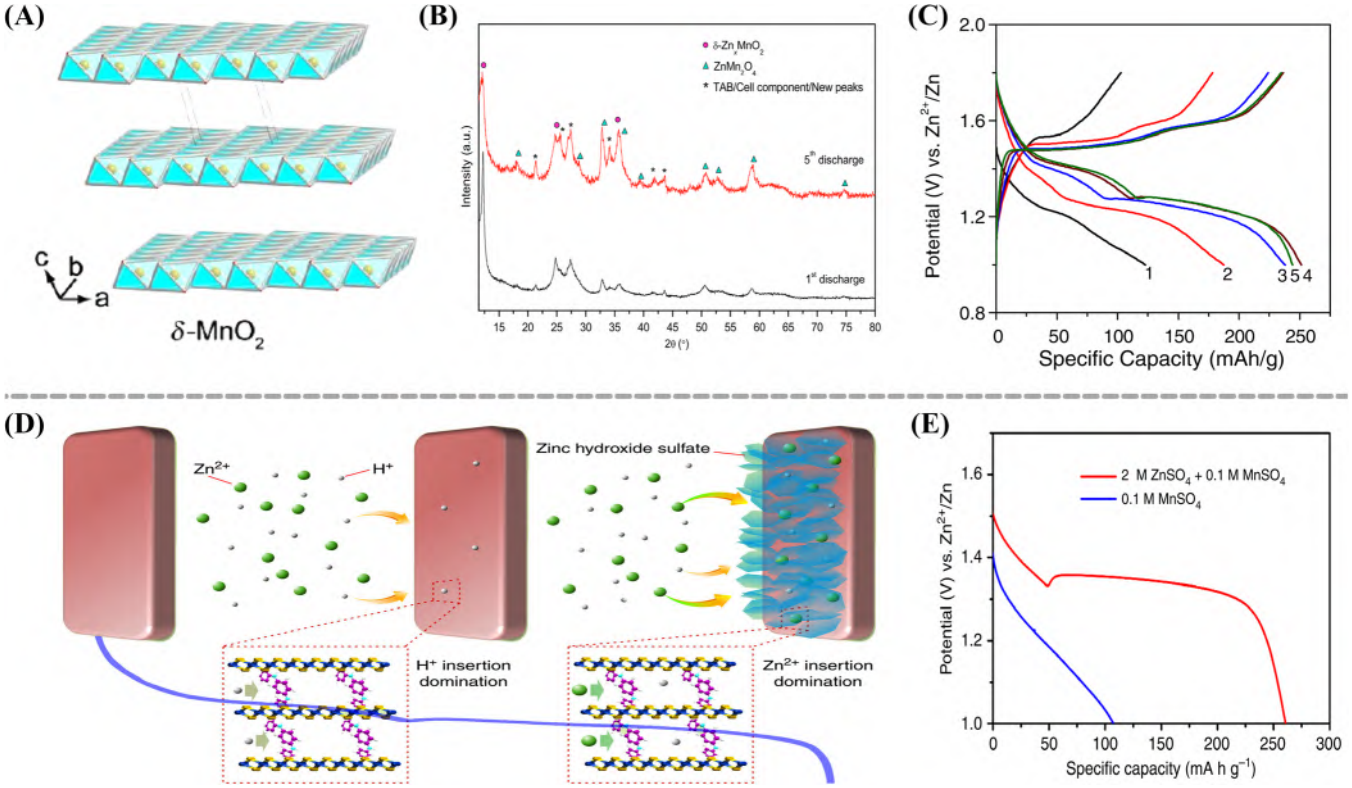

FIGURE 7 A, Crystallographic structure of δ-MnO_2. B, Ex-situ XRD patterns of the cathodes recovered from the Zn/δ-MnO_2 cells after first and fifth discharge cycle. C, Initial five voltage profiles of the δ-MnO_2 cathode vs zinc. Reproduced with permission from Ref. 112, Copyright 2015, Elsevier Ltd. D, Diagram showing the sequential insertion of H^+ and Zn^{2+}. E, The discharge profile of polyaniline (PANI)-intercalated MnO_2 electrode at current density of 50 mA/g in different electrolytes (red curve: 2 M $ZnSO_4$ + 0.1 M $MnSO_4$, blue curve: 0.1 M $MnSO_4$). Reproduced with permission from Ref. 113, Copyright 2018, Nature Publishing Group

2.1.6 | δ-MnO_2

Layered-type MnO_2 (δ-MnO_2), a two-dimensional infinite layer, is constructed by co-angled [MnO_6] octahedrons (Figure 7A). Due to controllable synthesis and high theoretical energy densities, layered δ-MnO_2 have been extensively studied in LIBs, SIBs, etc.[114,115] Lately, layered δ-MnO_2 has also aroused interest from researchers as cathode materials for ZIBs, which exhibits outstanding battery performances benefiting from the large interlayer distance (approximately 7.0 Å) of δ-MnO_2.[83] Kim et al[112] synthesized a flake-like δ-MnO_2 with about 200 nm in diameter via a facile thermal decomposition. The aqueous ZIBs with δ-MnO_2 cathode showed a discharged capacity of 250 mAh/g with two discharge plateaus at average voltages of 1.38 and 1.23 V (Figure 7C). Furthermore, the researchers revealed spinel-type $ZnMn_2O_4$ and layered-type δ-Zn_xMnO_2 form during discharge (Figure 7B). Unfortunately, layered δ-MnO_2 suffers capacity fading. Hence, it is necessary to in-depth study reaction mechanism of layered δ-MnO_2 upon discharge/charge, which is essential to improve the battery performances. Subsequently, Kim et al[116] revealed that capacity fading is caused by the production of irreversible spinel-type $ZnMn_2O_4$ and manganese dissolution. Unfortunately, they have not conducted in-depth research on the energy storage mechanism of δ-MnO_2 as a cathode for ZIBs. Recently, Wang et al[113] proposed a new perspective on the energy storage mechanism of δ-MnO_2 as a cathode for ZIBs that the hydrated H^+/Zn^{2+} co-insertion occurs during the discharge process, accompanied by the formation and disappearance of flake-like ZHS on the surface of the δ-MnO_2 electrode. During the first discharge region, H^+ protons are gradually embedded in the interlayer of MnO_2, decreasing H^+ concentration around the δ-MnO_2 cathode. With the continuous decrease of H^+, Zn^{2+} insertion begins to occur instead of H^+ insertion, forming the second discharge region, accompanied by the formation of flake-like ZHS on the electrode surface due to the excess of OH^- (Figure 7D). As Figure 7E shows, PANI-intercalated MnO_2 delivers two discharge platforms in 2 M $ZnSO_4$ + 0.1 M $MnSO_4$ electrolyte (red curve), while a single-slope discharge profile was observed for the 0.1 M $MnSO_4$ electrolyte (blue curve). And this further illustrates that the second discharge platform is affiliated with Zn^{2+} insertion. Furthermore, the researchers found the PANI-reinforced layered structure could efficiently eliminate the structure collapse caused by the hydrated H^+/Zn^{2+} insertion,

achieving excellent cycle life along with high discharged specific capacity.

2.2 | Other manganese oxides

Apart from manganese dioxide, other manganese oxides may be also a suitable choice for the cathodes of ZIBs. Recently, some manganese oxides have been reported to achieve reversible (de)intercalation of Zn^{2+}, including Mn_2O_3, Mn_2O_4, Mn_3O_4. Among these materials, Mn_2O_3 (corrundum structure) was firstly reported by Kang et al[117] as a cathode material for rechargeable aqueous ZIBs, which exhibited reversible capacities of 148 mAh/g (Figure 8C). It was confirmed that a phase transition reaction between

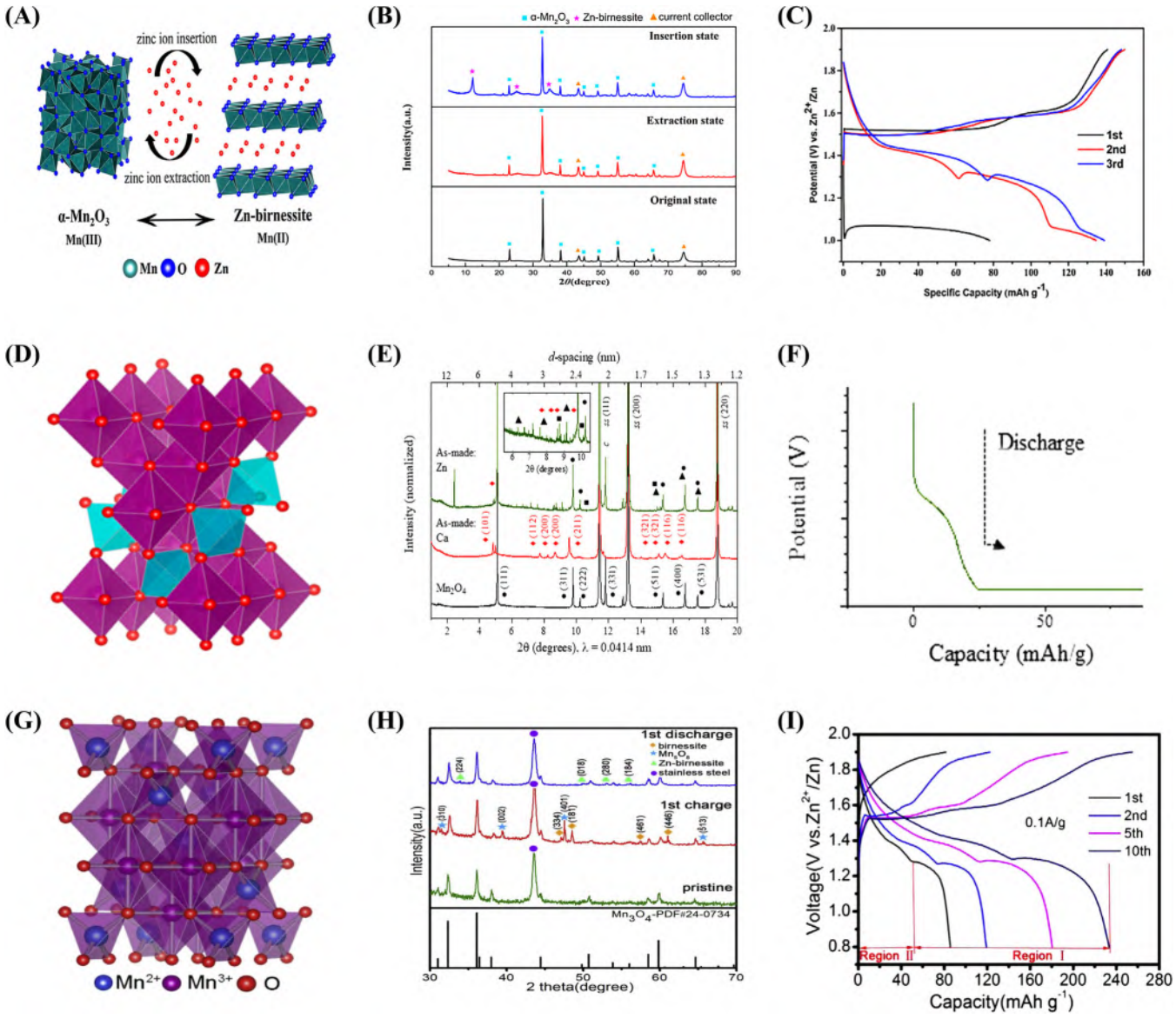

FIGURE 8 A, Schematics of α-Mn_2O_3 as cathode material for zinc-ion battery. B, XRD patterns of α-Mn_2O_3 cathode at original state, zinc-ion extraction state and zinc-ion insertion state. C, Galvanostatic charge-discharge curve of ZIB with α-Mn_2O_3 cathode in 2 M $ZnSO_4$ electrolyte. Reproduced with permission from Ref. 117, Copyright 2017, Elsevier Ltd. D, Crystallographic structure of as-prepared Mn_2O_4 material. E, Synchrotron powder X-ray diffraction of spinel Mn_2O_4: pristine (black), reduced to −0.4 V vs SCE in either Ca^{2+} (red) or Zn^{2+} (green) electrolyte. The upper *x*-axis illustrates the corresponding d-spacing values. Circles (●) correspond to cubic spinel Mn_2O_4, diamonds (◆) correspond to tetragonally distorted spinel like Mn_3O_4, represents the stainless-steel substrate, squares (■) correspond to ZnO, and triangles (▲) correspond to $Zn_2Mn_3O_8$. The inset represents a zoomed view of the host reduced in Zn^{2+} electrolyte between 5 and 10° (λ = 0.0414 nm). F, Zn^{2+} aqueous electrolytes at rate of C/40. Reproduced with permission from Ref. 118, Copyright 2018, ACS Publications. G, Crystallographic structure of as-prepared Mn_3O_4 material. H, Ex-situ XRD of Mn_3O_4 cathode at the first cycle. I, Galvanostatic charge–discharge curve of assembled Zn/2 M $ZnSO_4$/Mn_3O_4 battery. Reproduced with permission from Ref. 119, Copyright 2018, Elsevier Ltd

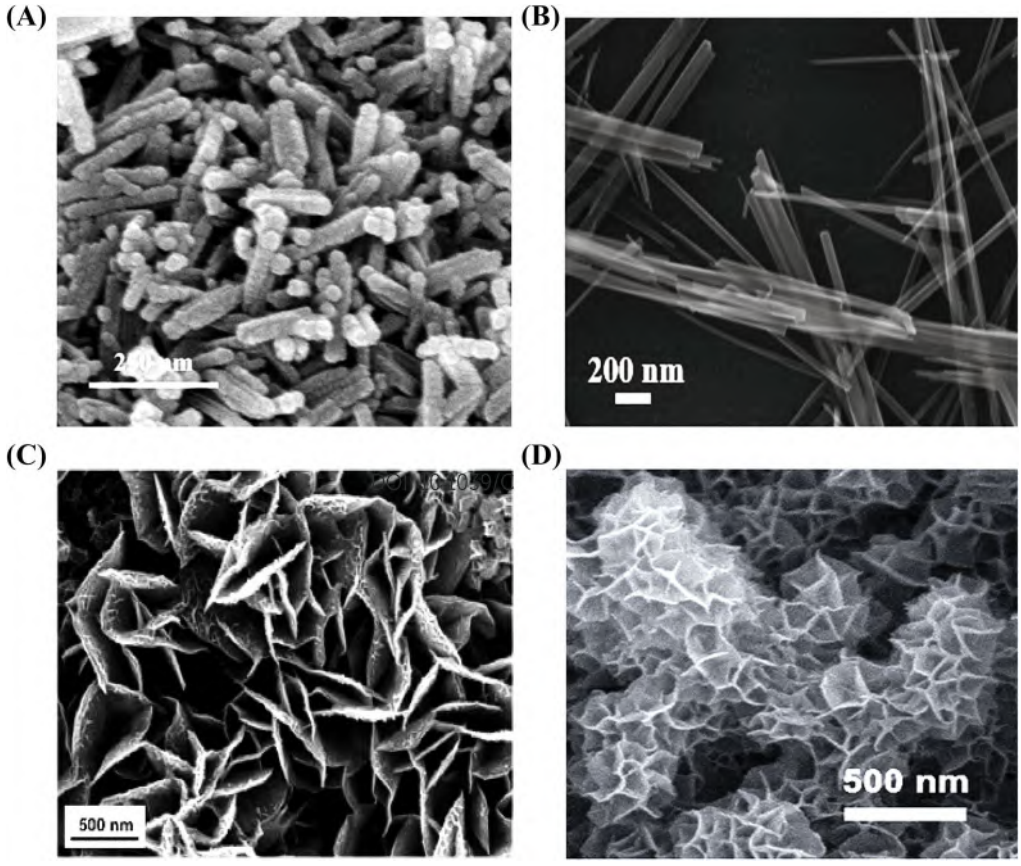

FIGURE 9 SEM image of, A, α-MnO_2 nanorods, reproduced with permission from Ref. 85, Copyright 2016, Elsevier Ltd. B, MnO_2 nanowires, reproduced with permission from Ref. 120, Copyright 2018, Wiley-VCH. C, cw-MnO_2 nanosheets, reproduced with permission from Ref. 121, Copyright 2019, The Royal Society of Chemistry. D, Mn_3O_4 flowers. Reproduced with permission from Ref. 122, Copyright 2018, American Chemical Society

Mn_2O_3 and layered-type Zn-birnessite occurs with Zn^{2+} insertion/extraction in electrode material (Figure 8A, B). In addition, Cabana et al[118] studied the zinc storage performance of a cubic spinel Mn_2O_4 (Figure 8D) cathode in an aqueous electrolyte. To our regret, the specific capacity is low and the potential is less than 1 V (Figure 8F). Interestingly, Figure 9E shows that during the discharge, Mn_2O_4 undergoes a partial structural transition to form tetragonal spinel, accompanied by the formation of layered MnO_2 containing structural water, ZnO, and $Zn_2Mn_3O_8$. It was speculated that Zn^{2+} can be embedded in Mn_2O_4, but pure zinc phase will preferentially generate near the Mn-rich particles.

Another spinel-type Mn_3O_4 (Figure 8G) was reported in ZIBs by Kang et al,[119] exhibiting discharged capacities of 239.2 mAh/g (Figure 8I). Here, an in-depth study was carried out to explore the reaction mechanisms of Mn_3O_4. Mn_3O_4 is firstly oxidized to Mn_5O_8 by oxidizing Mn^{3+} to Mn^{4+} and dissolving Mn^{2+} (Equation (16)). Next, Mn_5O_8 convert to birnessite with dissolving Mn^{2+} into the electrolyte and inserting H_2O (Equation (17)). Due to the incomplete electrochemical oxidation, Mn_5O_8 and birnessite coexist at the first charge. Upon discharge, Zn^{2+} intercalate into the interlayer of birnessite, forming Zn-birnessite accompanied by reducing Mn^{4+} to Mn^{3+}(Figure 8H). Of note, both MnOOH and ZHS phases are found, indicating a complex reaction mechanism.

$$2Mn_3O_4 \rightarrow Mn_5O_8 + Mn^{2+} + 2e^- \quad (16)$$

$$Mn_5O_8 + xH_2O \rightarrow 4MnO_2 + xH_2O + Mn^{2+} + 2e^- \quad (17)$$

Up to now, α-MnO_2, β-MnO_2, γ-MnO_2, δ-MnO_2, spinel-type MnO_2, todorokite-type MnO_2, and α-Mn_2O_3 have been reported as host materials for zinc-ion storage. Due to the various crystallographic polymorphs of manganese oxides, the electrochemical reaction mechanism of manganese oxides in neutral (or mild acid) electrolyte still remains controversial. Basically, zinc-ion insertion/extraction and proton insertion/extraction during the redox of manganese oxides are the two mainstream views. From the current overall research results, the energy storage mechanism of aqueous Zn-MnO_2 batteries is likely to be independent of the specific crystal structure, and multiple mechanisms coexist, including

Zn^{2+} insertion/extraction, proton insertion/extraction, and chemical conversion reaction. However, it is urgently needed for ingenious exploration and more in-depth research on the specific mechanism.

3 | THE STRATEGIES OF PERFORMANCE OPTIMIZATION FOR MANGANESE-BASED CATHODE MATERIALS

Due to high operating potential and specific capacity, manganese-based oxides are regarded as very promising cathode materials for ZIBs. Up to now, various manganese oxides, such as β-MnO_2, γ-MnO_2, α-MnO_2, Todorokite-Type MnO_2, ε-MnO_2, and δ-MnO_2, have been developed as cathode materials for aqueous ZIBs. Unfortunately, many challenges still exist in making great breakthroughs in high-performance manganese-based cathode materials for aqueous ZIBs, as follows: (a) All manganese oxides generally suffer from structure transformation, serious structural damage and large volume change during the repetitive intercalation/deintercalation of hydrated H^+/Zn^{2+} ions, leading to capacity fading of ZIBs. (b) Mn^{2+} ions are continuously dissolved from the manganese oxide cathodes into the electrolyte. (c) Manganese oxides often deliver poor electrical conductivity. Owing to these, manganese-based materials undergo unsatisfied electrochemical performance, such as bad cycle performance and inferior rate performance. To achieve high performance MZIBs, some strategies, including construction of nanostructures, compositing with conductive substrates, introduction of defects, adjustment of interlayer spacing, and optimization of electrolytes, have been reported.

3.1 | Construction of nanostructures

Nanostructured electrode materials with high specific surface area can promote foreign ion storage/release into/from the electrode material structure due to the improvement of the diffusion dynamics by shortening the diffusion distance of electron and ions transfer.[123,124] Currently, there are mainly four types for nanostructured electrode materials as follows: (a) zero-dimensional (0D) nanomaterials; (b) one-dimensional (1D) nanomaterials (such as nanotubes, nanowires, and nanorods); (c) two-dimensional (2D) nanomaterials (such as nanosheets and nanoplates); (d) Hierarchical nanomaterials constructed by 2D nanomaterials.[125-127] Generally, owing to the unique surface and structural characteristics, different dimensional nanomaterials exhibit diverse performances. 0D structure nanoparticles with a particle size below 100 nm possess short diffusion distance for inserted ion and large contact area with the electrolyte.[119,123] For example, Kang et al[91] successfully synthesized α-MnO_2 composed of spherical nanoparticles and cylindrical nanorods by a coprecipitation method, which delivered a specific surface area of 208 m^2/g and first discharge-specific capacity of 234 mAh/g. However, high specific surface energy can easily cause the aggregation of nanoparticles, resulting in poor cycle performance. Compared with 0D structured nanoparticles, 1D structured materials (eg, nanotube, nanowire, and nanorod) not only have short ion diffusion distance in the radial direction, but also enable rapid electronic transmission in the ID direction.[128-130] Kim et al[85] prepared MnO_2 nanorod with a large specific surface area of 153 m^2/g via a simple solvent-free synthesis method, achieving first discharge specific capacity of 323 mAh/g (Figure 9A). Another 1D-structured MnO_2 nanowires were synthesized by Mai et al,[120] which exhibited an enhanced discharge capacity of 362.2 mA h/g (Figure 9B). However, specific surface area and porosity of 1D structured materials are nonadjustable, limiting their application. Compared with 0D and 1D nanomaterials, 2D nanomaterials possess the wide interlayer spacing between nanosheets, the large surface-to-volume ratio, and the atomic thickness, making them show more effectively active sites and remarkable mechanical flexibility.[131,132] Choi et al[121] synthesized layered MnO_2 nanosheets, which delivered a large discharge capacity of 350 mAh/g (Figure 9C). Nevertheless, 2D nanomaterials are inclined to stack or agglomerate, which severely limits the contact of electrolyte with electrode material. One effective method to solve this problem is to build a hierarchy. Addition to maintaining the advantages of 2D nanomaterials, the hierarchical structure with 2D nanomaterials as a unit can also obtain other structural characteristics at different scales, such as large size, high porosity, remarkable specific surface area and excellent permeability.[133,134] Inspired by this, Liang et al[122] reported Mn_3O_4 flowers, which delivered higher specific capacity of 296 mA h/g and excellent cycle stability without capacity fading after 500 cycles (Figure 9D).

3.2 | Compositing with conductive substrates

Generally, manganese-based oxides show intrinsic low electrical conductivity and large volume change induced by Zn^{2+} (de)intercalation during the charge and discharge cycle, resulting in poor electrochemical performance. Compositing with conductive substrate is considered to be a resentful way to enhance the conductivity and stability of manganese-based oxides, including carbon nanotubes (CNTs), graphene, carbon fiber paper (CFP), and stainless steel welded mesh (SSWM), etc.

CNTs have a tubular structure, showing a much high length-to-diameter ratio, typically several nanometers in diameter and many micrometers in length. Due to remarkable electroconductibility and large specific surface area, CNTs is supported to be a perfect conductive substrate for manganese-based materials.[135-138] Kang et al[139] synthesized the MnO_2 nanorod/acid-treated α-CNT composites by coprecipitation way (Figure 10A), which displayed both excellent storage properties of 665 mAh/g at 0.1 A/g (400 mAh/g at 1A/g) and reversibility at various current rates (Figure 10B, C). In addition, the researchers found that acid-treated CNTs with large specific surface area and a lot of oxygen-containing functional groups (eg, carboxyl group, hydroxyl group, etc.), cannot only be tightly bonded to MnO_2 to build MnO_2/α-CNT composites, but also serve as additional sites for Zn^{2+} ions to increase the reversible capacity. Compared with CNTs, graphene has superior conductivity and specific surface area, which can enhance the electroconductibility of the cathode and act as a buffer support to accommodate volume changes induced by Zn^{2+} (de) intercalation during the charge and discharge cycle.[138,140] Mai et al[120] proposed α-MnO_2 nanowire scroll-coated by graphene (Figure 10D), which delivered high discharge capacity of 362.2 mA h/g after 100 cycles and excellent rate performance compared with that of bare MnO_2 nanowire (MNW) (Figure 10E, F).

Different from CNTs and graphene, the 3D substrates (such as carbon fiber paper and SSWM) not only can

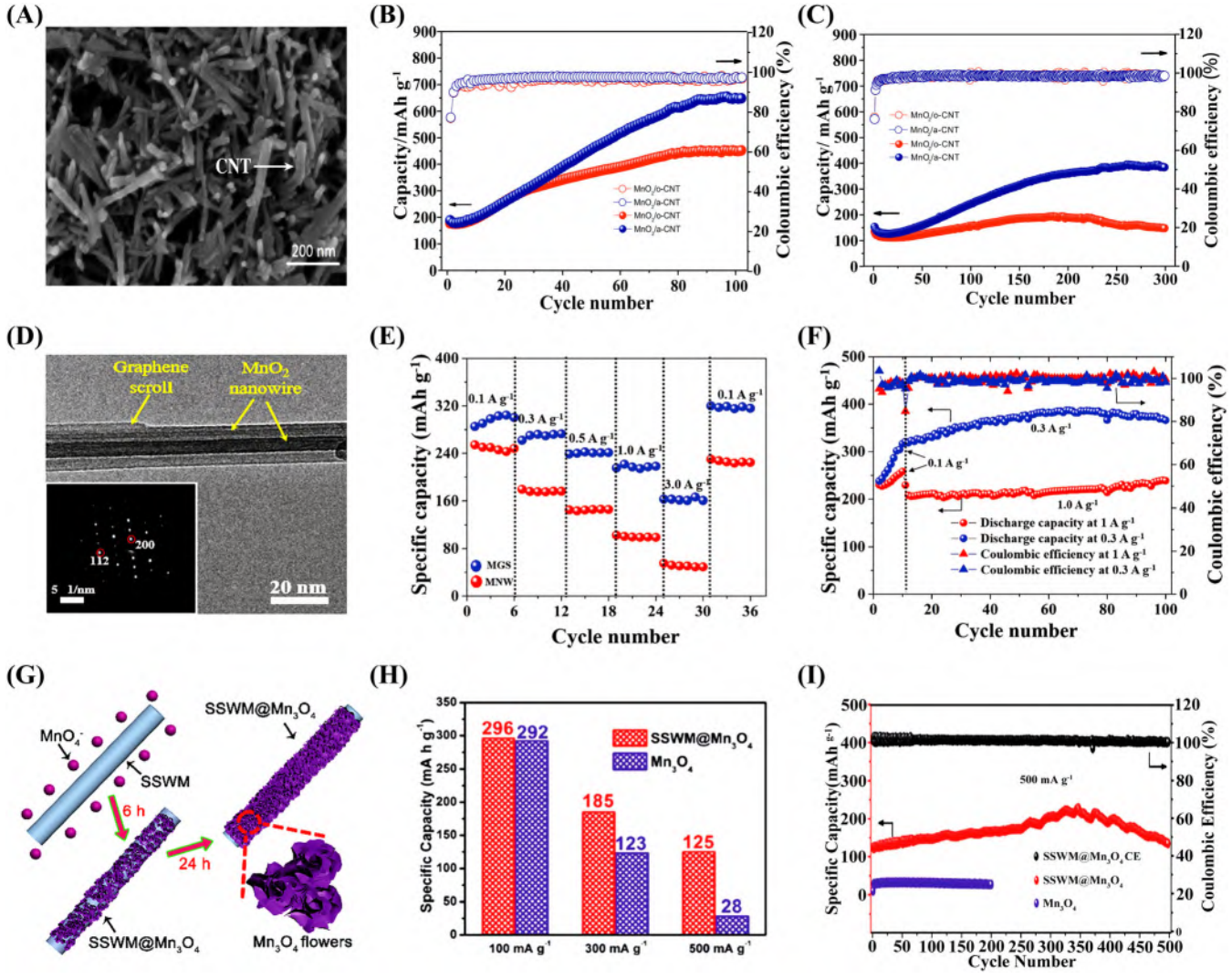

FIGURE 10 A, SEM image of the MnO_2/α-CNT nanocomposites. Cycling performance of the MnO_2/CNT and MnO_2/o-CNT electrode in 2 mol/L $ZnSO_4$ and 0.5 mol/L $MnSO_4$ hybrid aqueous electrolyte at the current density of, B, 0.1 A/g, C, 1 A/g. Reproduced with permission from Ref. 136 Copyright 2014, Elsevier Ltd. D, TEM images and SAED inset in G of MGS. E, Rate performances of MGS and MNW. F, Cycling performances of MGS at 0.3 and 1 A/g after an activation process at 0.1 A/g. Reproduced with permission from Ref. 120, Copyright 2018, Wiley-VCH. G, Synthesis schematic of SSWM@Mn_3O_4. Performance comparison of SSWM@Mn_3O_4 and Mn_3O_4: H, Capacity at different current densities and I, cycle performance at 500 mA/g. Reproduced with permission from Ref. 122, Copyright 2018, American Chemical Society

improve the conductivity of the electrode, but also offer the support for the active material to form a stable porous structure.[138,141-144] Recently, a MnO_2@CFP cathode was constructed by electrodeposition, which can cycle 1000 time at a high rate of 6.5 C with a low capacity decay rate of 0.007% per cycle for 10 000 cycles.[110] Moreover, Liang et al[122] reported a SSWM@Mn_3O_4 composite. Compared to Mn_3O_4 powder, the SSWM@Mn_3O_4 delivered higher specific capacity of 296 mA h/g and excellent cycle stability (Figure 10H, I).

3.3 | Introduction of defects

Some irregularity or imperfection of particle arrangement in a crystal structure is defined as the crystal defect, which imparts new properties to the material, including electrical, magnetic and optical properties.[145-150] Generally, manganese oxides have low utility rate of active sites on their surface, greatly limiting their application in ZIBs. In this case, introducing oxygen vacancy in manganese oxides could reduce Gibbs free energy of Zn^{2+} adsorption around the defects, achieving high Zn^{2+} adsorption/desorption reversibility (Figure 11A). Recently, Lee et al[151] prepared σ-MnO_2 with oxygen defects (O_d-MnO_2), achieving a satisfactory discharge capacity as high as 345 mAh/g and superior rate capability in aqueous ZIBs (Figure 11C, D). Furthermore, it was confirmed that Zn^{2+} storage in σ-MnO_2 may be attributed to diffusive component (de/intercalation of Zn^{2+} into/from the interlayer), and capacitive component (reaction mechanism: $xZn^{2+} + 2xe^- + MnO_2 \rightarrow MnOOZn_x$, forming the double electro-layer) (Figure 11B). When as the cathode in rechargeable aqueous ZIBs, the O_d-MnO_2 delivered high capacities of 345 mAh/g and superior rate capability (Figure 11C, D).

Compared with monovalent alkali ions, Zn^{2+} suffers huge electrostatic repulsion during the de/intercalation into/from manganese oxides due to its higher valence state.[152] Theoretically, generating cation vacancies in manganese oxides could reduce the electrostatic repulsion for inserted Zn^{2+}, enabling high migration of Zn^{2+} and consequently fast electrode dynamics. Inspired by this, Chen et al[153] fabricated a cation-defective $ZnMn_2O_4$ spinel by a two-step method. Although the ideal $ZnMn_2O_4$ is not conducive to the intercalation of Zn^{2+} ions, the vacant-rich $ZnMn_2O_4$ can achieve a good reversible (de)intercalation of Zn^{2+} due to the weak electrostatic barrier caused by Mn vacancies. When as the cathode in aqueous ZIBs, the cation-defective $ZnMn_2O_4$ exhibited reversible discharged capacities of 150 mAh/g and excellent circulation stability.

Addition to vacancies, cationic doping is considered as a smart strategy to enhance the energy storage performance of manganese oxides when as electrode in supercapacitors and

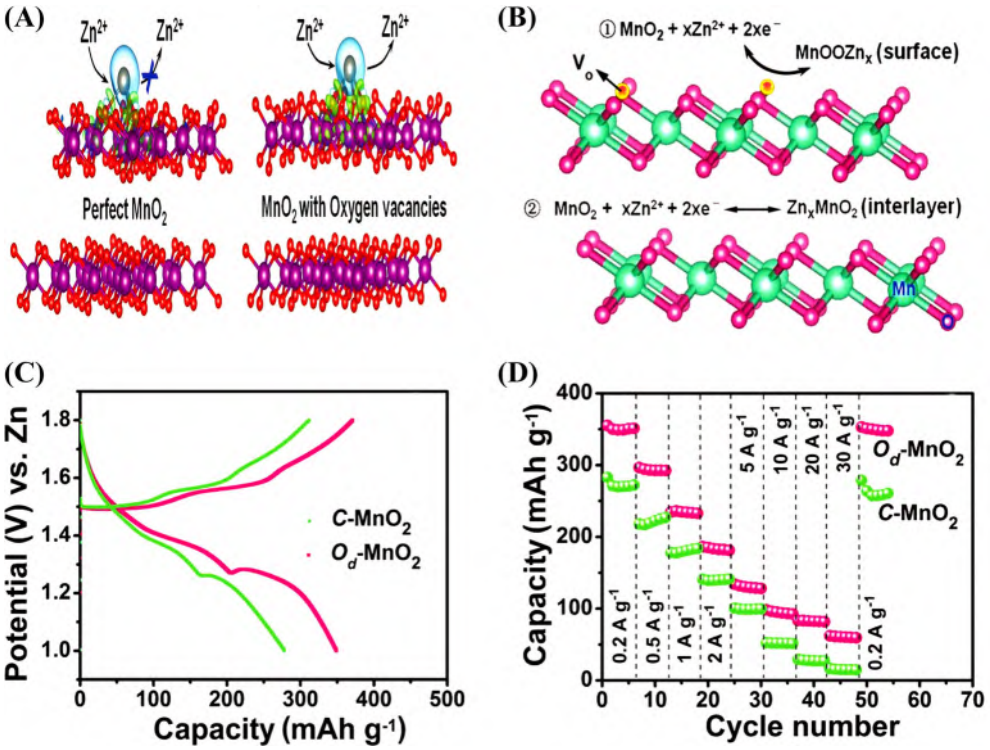

FIGURE 11 A, The schematic illustration of Zn^{2+} adsorption/desorption. B, Schematic illustration of oxygen-deficient σ-MnO_2 for Zn ion storage. Electrochemical performance of Zn/Od-MnO_2 and Zn/C-MnO_2 cells: C, discharge/charge profiles at current densities of 0.2 A/g; D, rate performances. Reproduced with permission from Ref. 148, Copyright 2019, Wiley-VCH

LIBs. Hu et al[154] reported a V-doped MnO_2 with enhanced conductivity for supercapacitor applications, achieving remarkable cycle stability and enhanced electrochemical performances. Furthermore, Julien et al[155] confirmed doping Sn in MnO_2 can enhance the capacity retention and the rechargeability of MnO_2 as electrode for LIBs. Subsequently, Liu et al[156] confirmed that doping iron in MnO_2, causing anisotropic changes in lattice parameters, could increase the discharged capacity for LIBs at high rates. Inspired by these, Kim et al[157] prepared a V-doped MnO_2 at ambient temperature as the cathode for ZIBs. Due to increased specific surface area and enhanced electronic conductivity induced by V doping, the cathode delivered high discharged capacities and superior cycling performance compared to the pure MnO_2 electrode.

3.4 | Adjustment of interlayer spacing

Although the radius of zinc ions is very similar to that of lithium ions, the radius of hydrated zinc ions is larger than that of lithium, sodium, and potassium. Therefore, many traditional layered materials cannot satisfy the storage of zinc ions. As a result, the regulation of layer spacing has become a very attractive strategy for optimizing the performance of layered electrode materials.

Just like the cases in Mg-ion battery and Na-ion battery, the structural water cannot only enlarge the interlayer spacing, but also effectively shield the electrostatic interactions between the foreign cation and the host framework. As a benefit, the diffusion of the foreign cation in the host is promoted, helping to stabilize the host structure during cycling. Recently, Choi et al[121] reported layered MnO_2 with structure water (cw-MnO_2) as the cathode of aqueous ZIBs (Figure 12B, C). To determine the effect of the crystal water, the researchers tested the battery performances of cw-MnO_2 containing different amount of water (Figure 12A). And they found that cw-MnO_2 with 0.94 water molecules had the best performance of the capacity of 350 mAh/g (Figure 12D-F), reaching a conclusion that the advisable interlamellar spacing and high water content can help to realize acceptable cyclic performance through suppressing Mn dissolution and maintaining the electrode structure stable during cycling. However, it is uncertain that how much structural water is most suitable. Although content of structural water can promote the fast diffusion of Zn^{2+}, it will also lead to structural instability, affecting its electrochemical performance. Therefore, it is important and meaningful to explore and build the dependence of the electrochemical performance and layer spacing of manganese-based materials on the amount of structural water.

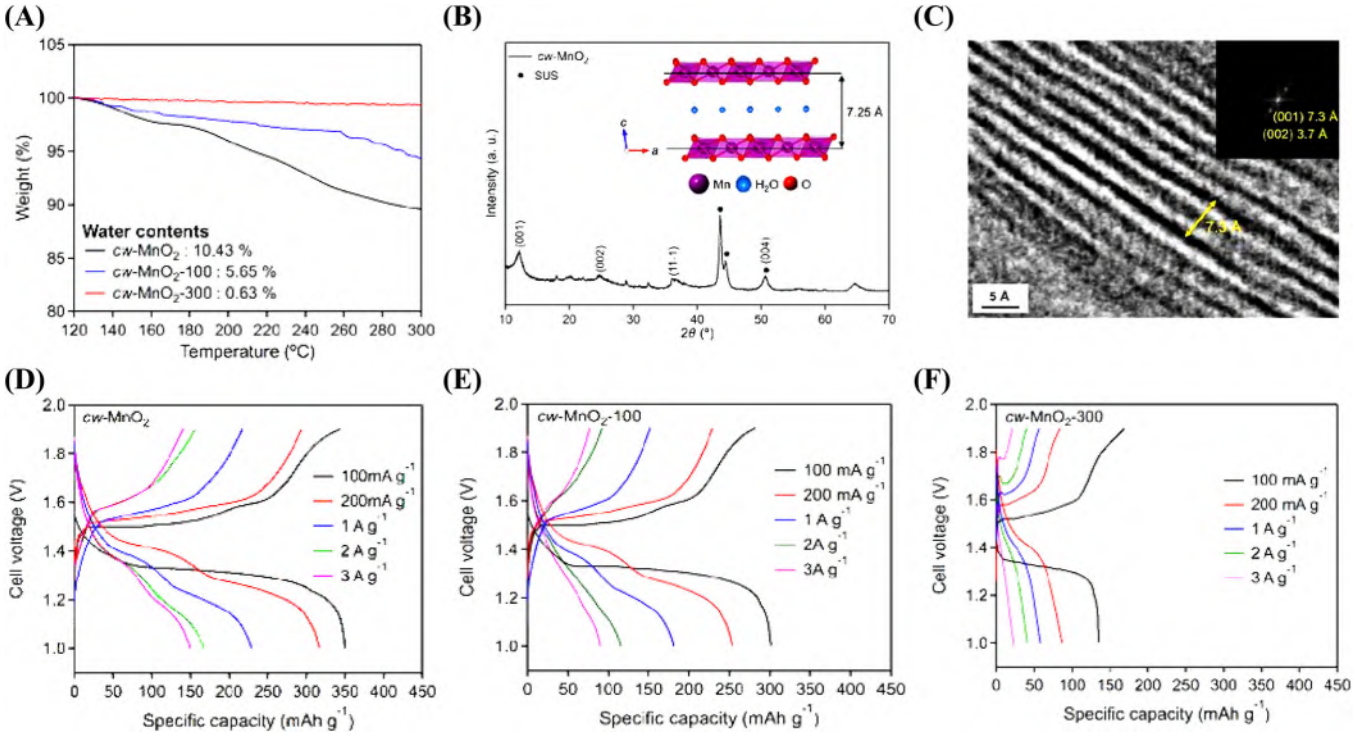

FIGURE 12 A, TGA profiles of pristine cw-MnO_2, cw-MnO_2-100, and cw-MnO_2-300. B, XRD pattern and (inset) crystal structure of cw-MnO_2. C, ABF-STEM images of cw-MnO_2 at high magnifications Discharge/charge voltage profiles at various current densities for D, pristine cw-MnO_2, E, cw-MnO_2-100, and F, cw-MnO_2-300. Reproduced with permission from Ref. 121, Copyright 2019, American Chemical Society

Apart from structural water, other inserted metal ions (Na^+, K^+, and Mg^{2+}, etc.) and polymer molecule (polyaniline) have also been proved to be an efficient way to adjust interlayer spacing and maintain structural stability.[36,60,158-160] Recently, Wang et al found that the interlayer spacing of manganese dioxide pre-embedded with sodium ions was expanded to approximately 0.727 nm, showing a capacity of 266 mAh/g. Wherein, the Na^+ serve as pillars to stabilize the structure, enhancing Zn^{2+} storage ability and achieving long-cycle stability. In addition, a polyaniline-intercalated layered MnO_2 was also reported to show high capacity and excellent cycle stability because polymer-strengthened layered structure (approximately 1.0 nm) could eliminate phase changes and facilitate charge storage.[113]

3.5 | Optimization of electrolytes

Electrolyte is recognized as a key component affecting the electrochemical performance of MZIBs. Currently, the $ZnSO_4$ aqueous solution is used as the electrolyte of most ZIBs because of its excellent electrochemical properties.[161] However, it requires a long activation process for the battery to achieve maximum specific capacity, and its cycle stability is not ideal.[62] Subsequently, the $Zn(CF_3SO_3)_2$ solution attracts great attention due to its excellent electrochemical performance, such as high ionic conductivity, rapid kinetics and remarkable stability of Zn plating/stripping. In addition, the researchers also bring to light a fact that the bulky $CF_3SO_3^-$ anion could facilitate Zn^{2+} ions transportation in the electrode by decreasing the number of water molecules surrounding Zn^{2+} cations and reducing the solvation effect. However, there are still two important challenges for the above two electrolytes to achieve the commercial application of MZIBs, as follows: (a) Due to the weakly acidic of $ZnSO_4$ or $Zn(CF_3SO_3)_2$ aqueous electrolyte, most manganese oxides or other manganese-based materials will slowly dissolve into electrolytes. It is not negligible for the impact on battery performance, especially when mass-produced after commercialization. (b) Theoretically, the aqueous ZIBs generally exhibit low potential due to the narrow electrochemical window of the aqueous solution.[56,58,70]

In this case, adding additives is proved to effectively inhibit the dissolution of manganese-based materials. For example, in Zn-MnO_2 cell, when $MnSO_4$ is added into $ZnSO_4$ electrolyte, the dissolution of α-MnO_2 is relieved because it can change the dissolution equilibrium of Mn^{2+} from α-MnO_2 electrodes.[102] Recently, $Zn(CF_3SO_3)_2$ electrolyte containing additive $Mn(CF_3SO_3)_2$ additive has been reported to exhibit better performance than $ZnSO_4$ electrolyte with $MnSO_4$ in suppressing manganese dissolution.[62]

Furthermore, for matching manganese-based electrodes with high potential in the future, the electrolytes with high O_2 reduction potential are considered to be a very effective way to obtain high potential ZIBs. Compared to the conventional electrolytes discussed above, water in salt electrolyte may be a very suitable choice to broaden the voltage window of aqueous ZIBs because of the low water activity.[162] Unfortunately, the high concentrated electrolyte often show unsatisfied capacity and rate capability induced by poor ion diffusion kinetics. Recently, gel electrolytes have been greatly developed in flexible ZIBs due to outstanding mechanical properties. Moreover, it has been confirmed that gel electrolyte can also effectively increase the potential of the battery.[57]

4 | FLEXIBLE ZIBS BASED ON MANGANESE-BASED CATHODE MATERIAL

With growing requirement of cheapness and high security energy storage device for wearable and flexible electronics,[163-170] aqueous MZIBs have been regarded as a favorable choice because of high safety and environmental friendliness. To achieve stable electrochemical performance under various deformations, all parts of the battery should meet the required flexibility. However, the conventional coin-type MZIB cannot accord with this requirement due to its rigid design. In this context, a flexible MZIB with liquid electrolyte was assembled by Zhou et al.[171] In this battery, the flexibility is achieved by depositing both Zn and cathode material on carbon clothes. However, the conventional liquid electrolytes are not suitable for flexible systems because of their volatilization and leaking problems. Inspired by this, flexible solid-state rechargeable MZIBs have been developed to replace the conventional flexible MZIBs. And flexible solid-state MZIBs will be a trend in the development of MZIBs applications.

For the practical application of flexible MZIBs, it is a key to find a polymer electrolyte that is stable, highly ionic conductive and easy to process. In addition, this electrolyte can process the battery into any shape and avoid electrolyte leakage. Considering these factors, Tong et al[172] first assembled flexible quasi-solid-state rechargeable ZIBs including zinc anode, MnO_2@poly(3,4-ethylenedioxythiophene) (PEDOT) cathode, and optimized polyvinyl alcohol (PVA) gel electrolyte, which exhibited a high discharge capacity of 366.6 mA h/g. However, the PVA-type electrolytes sustain poor flexibility, low ion-conductivity, and unsatisfactory mechanical properties. Contrastively, the hydrogel with hydrophilous polymer network structure, which can swell with a lot of water molecules, could dissolve various kinds of ions, thus making it an excellent ionic conductor. In this case, Zhi et al[173] demonstrated an ultra-safe solid-state rechargeable and flexible MZIB using a hierarchical gelatin

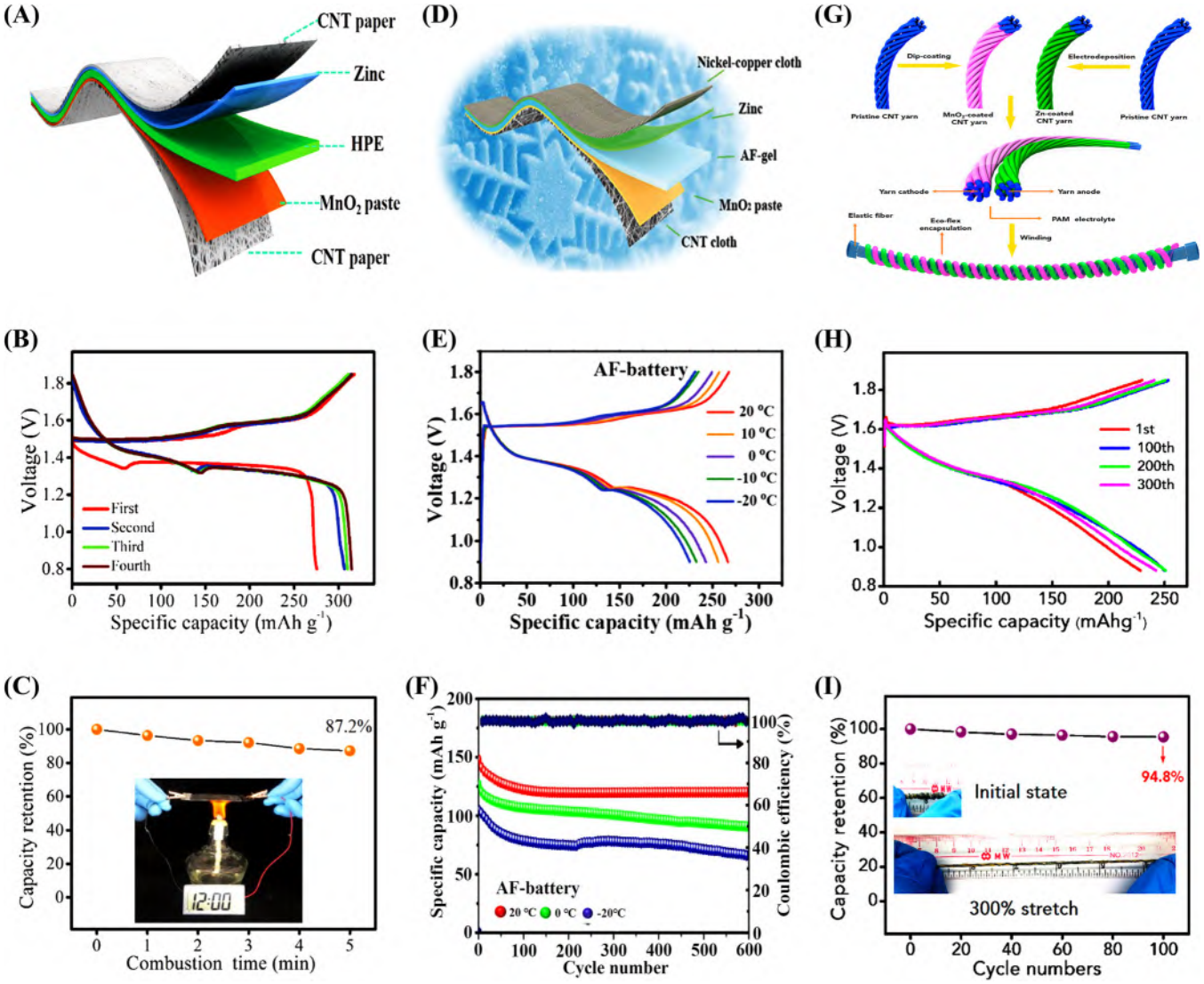

FIGURE 13 A, Schematic illustration of the structure of the solid-state ZIB. B, Galvanostatic charge/discharge profiles at initial four cycles (61.6 mA/g). Electrochemical performance of the solid-state rechargeable ZIB in C, Combustion test. Reproduced with permission from Ref. 164, Copyright 2018, American Chemical Society. D, Schematic illustration of the structure of the AF-battery. E, GCD curves of the AF-battery at a current density of 0.2 A/g. F, Extended cycling performance at 2.4 A/g of the AF-battery at different temperatures. Reproduced with permission from Ref. 166, Copyright 2019, American Chemical Society. G, Schematic diagram of fabrication and encapsulation of the yarn ZIB. H, Discharge curves of the yarn ZIB after different bending cycles. I, Dependence of capacity retention on cycle numbers with a strain of 300%. For H and I, tests were performed at a current density of 0.3 A/g. Reproduced with permission from Ref. 168, Copyright 2018, ACS Publications

and PAM-based electrolyte (Figure 13A). Thanks to ingenious designs of all parts of the battery, the flexible solid state MZIB delivered high discharge specific capacity of 306 mAh/g (Figure 13B). In addition, compared to previous reports, this solid MZIB can offer higher wearability and higher security, and operate well in different harsh conditions. For example, the solid MZIB still exhibited excellent electrochemical performance at high temperatures (Figure 13C). Later, Li et al[174] assembled a rechargeable Zn-ion battery with the gum bio-electrolyte, which can deliver competitive performance including high capacities, superior rate capability, excellent cycle stability, and flexibility. Here, the stable, highly conductive gum bio-electrolyte was synthesized by dissolving xanthan gum in aqueous $ZnSO_4/MnSO_4$ solution, which greatly simplified the preparation process of gel-like electrolyte. Moreover, the researchers found that dendritic growth can be inhibited in the gum electrolyte. Nevertheless, the conventional hydrogel electrolyte will suffer poor electrochemical performance and flexibility due to freezing at lower temperatures. In this end, Zhi et al[175] introduced an anti-freezing aqueous Zn-MnO_2 battery (AF-battery) using a special electrolyte (Figure 13D). The AF-battery still delivered high discharge capacity of 226 mA h/g and excellent cycle

stability under the extremely cold temperature of −20°C (Figure 13E, F).

Compared with 2D structure battery, 1D fiber or yarn type battery with unique advantages of miniaturization, adaptability, and weavability is considered to be more suitable for smart or wearable textile applications. Recently, Zhi et al[176] reported a wire-shaped flexible ZIBs with shape memory function, achieving acceptable capacity of 143.2 mAh/g. The battery has a shape-memory function that can maintain its shape and electrochemical properties against the effects of mechanical deformation. In practical applications of wearable devices, batteries must have excellent ductility. For nonelastic batteries, when they are stretched, the internal connection of the conductive material is broken, resulting in a decrease in electrical conductivity. In contrast, the elastic battery is the perfect solution to this problem due to its excellent ductility. Recently, ID flexible Zn/MnO_2 battery composed of coiled-coil yarn cathode and PAM type polymer electrolyte was assembled by Zhi et al,[177] achieving a high specific capacity of 302.1 mA/g (Figure 13G, H). Surprisingly, the solid-state yarn ZIBs exhibited excellent ductility, and they still showed a high capacity retention rate under high strain (Figure 13I), making them ideal and hopeful energy storage technologies in flexible wearable devices.

5 | SUMMARY AND OUTLOOK

Currently, aqueous MZIBs are being developed as an ideal candidate for large-scale energy storage because of their cheapness, high security, eco-friendliness, low toxicity, facile fabrication, and excellent electrochemical performance. However, there are still many challenges to achieving commercial application of MZIBs. Here, the in-depth study of valuable study directions could play guidance for aqueous MZIBs, as follows:(a) Accurate understanding of zinc storage mechanism. Although there are many studies on the mechanism of zinc storage in manganese-based materials, the specific mechanism of zinc storage remains controversial. (b) Further exploration of the dissolution and deposition of manganese during charge and discharge. It is well-known that the dissolution and deposition of manganese is a common problem in manganese-based cathode materials, which is one of the important factors leading to the capacity decay of the manganese-based electrodes. Subsequently, it has been proposed to add manganese sulfate or manganese trifluoromethanesulfonate as an additive to achieve a balance of dissolution and deposition of manganese by inhibiting the dissolution of manganese. However, recent reports on the preparation of manganese-based cathode materials by electrodeposition have led to another question: whether the addition of additives will cause the deposition of manganese to be greater than the dissolution, resulting in changes in the quality of the cathode material? Therefore, further research on the dissolution and deposition of manganese during charging and discharging is very urgent and meaningful. (c) Performance optimization for manganese-based cathode materials. Although many optimization methods for manganese-based cathode materials have been proposed, more stable and advanced optimization strategies are still needed. (d) Design of flexible ZIBs with manganese-based oxides as cathode material. With the rapid development of wearable and flexible electronic devices, the flexible energy storage technologies will usher in a very great opportunity. Although flexible zinc-manganese batteries are considered to be promising flexible batteries for flexible electronic devices due to low cost, abundant reserves, environmental protection, and low toxicity, there are still many key problems to hinder the commercialization of flexible MZIBs, such as lack of suitable electrolyte with wide operating temperature range and high-voltage.

ACKNOWLEDGMENTS

This work was financially supported by This work was financially supported by the National Natural Science Foundation of China (21725103 and 51631004), National Key R & D Program of China (2016YFB0100103, 2017YFA0206704), People's Government of Jilin Province Science and Technology Development Plan Funding Project (20180101203JC), and Changchun Science and Technology Development Plan Funding Project (18DY012, 19SS010), the Program for the JLU Science and Technology Innovative Research Team (2017TD-09).

CONFLICT OF INTEREST

The authors declare no conflict of interest.

REFERENCES

1. Dunn B, Kamath H, Tarascon JM. Electrical energy storage for the grid: a battery of choices. *Science*. 2011;334(6058): 928-935.
2. Yang Z, Zhang J, Kintner-Meyer MCW, et al. Electrochemical energy storage for green grid. *Chem Rev*. 2011;111(5):3577-3613.
3. Larcher D, Tarascon JM. Towards greener and more sustainable batteries for electrical energy storage. *Nat Chem*. 2015;7:19-29.
4. Zhai Y, Dou Y, Zhao D, Fulvio PF, Mayes RT, Dai S. Carbon materials for chemical capacitive energy storage. *Adv Mater*. 2011;23(42):4828-4850.
5. Yang CJ, Jackson RB. Opportunities and barriers to pumped-hydro energy storage in the United States. *Renew Sust Energ Rev*. 2011;15(1):839-844.
6. Simon P, Gogotsi Y. Materials for electrochemical capacitors. *Nat Mater*. 2008;7(11):845-854.

7. Liu J, Zhang JG, Yang ZG, et al. Materials science and materials chemistry for large scale electrochemical energy storage: from transportation to electrical grid. *Adv Funct Mater*. 2013;23(8): 929-946.
8. Qu DY. Studies of the activated carbons used in double-layer supercapacitors. *J Power Sources*. 2002;109(2):403-411.
9. Jiang J, Li YY, Liu JP, Huang X, Yuan C, Lou XWD. Recent advances in metal oxide-based electrode architecture design for electrochemical energy storage. *Adv Mater*. 2012;24(38):5166-5180.
10. Tarascon JM, Armand M. Issues and challenges facing rechargeable lithium batteries. *Nature*. 2001;414:359-367.
11. Saidur R, Rahim NA, Hasanuzzaman M. A review on compressed-air energy use and energy savings. *Renew Sust Energ Rev*. 2010;14(4):1135-1153.
12. Bolund B, Bernhof H, Leijon M. Flywheel energy and power storage systems. *Renew Sust Energ Rev*. 2007;11(2):235-258.
13. Armand M, Tarascon JM. Building better batteries. *Nature*. 2008; 451:652-657.
14. Hwang JY, Myung ST, Sun YK. Sodium-ion batteries: present and future. *Chem Soc Rev*. 2017;46(12):3529-3614.
15. Häupler B, Wild A, Schubert US. Carbonyls: powerful organic materials for secondary batteries. *Adv Energy Mater*. 2015;5(11): 1402034.
16. Muldoon J, Bucur CB, Gregory T. Quest for nonaqueous multivalent secondary batteries: magnesium and beyond. *Chem Rev*. 2014;114(23):11683-11720.
17. Xu CJ, Chen YY, Shi S, et al. Secondary batteries with multivalent ions for energy storage. *Sci Rep*. 2015;5:14120.
18. Etacheri V, Marom R, Elazari R, Salitra G, Aurbach D. Challenges in the development of advanced Li-ion batteries: a review. *Energy Environ Sci*. 2011;4(9):3243-3262.
19. Li Z, Huang J, Liaw BY, et al. A review of lithium deposition in lithium-ion and lithium metal secondary batteries. *J Power Sources*. 2014;254:168-182.
20. Wang QS, Sarkar A, Wang D, et al. Multi-anionic and -cationic compounds: new high entropy materials for advanced Li-ion batteries. *Energy Environ Sci*. 2019;12(8):2433-2442.
21. Liu JL, Xu CH, Chen Z, Ni SB, Shen ZX. Progress in aqueous rechargeable batteries. *Green Energy Environ*. 2018;3(1):20-41.
22. Li W, Dahn JR, Wainwright DS. Rechargeable lithium batteries with aqueous electrolytes. *Science*. 1994;264(5162):1115-1118.
23. Yang XY, Xu JJ, Chang ZW, et al. Blood capillary-inspired, free-standing, flexible, and low-cost super-hydrophobic N-CNTs@SS cthodes for high-capacity, high-rate and stable Li-air batteries. *Adv Energy Mater*. 2018;8(12):1702242.
24. Abouimrane A, Dambournet D, Chapman KW, Chupas PJ, Weng W, Amine K. A new class of lithium and sodium rechargeable batteries based on selenium and selenium−sulfur as a positive electrode. *J Am Chem Soc*. 2012;134(10):4505-4508.
25. Hueso KB, Armand M, Rojo T. High temperature sodium batteries: status, challenges and future trends. *Energy Environ Sci*. 2013;6(3):734-749.
26. Luo C, Xu YH, Zhu YJ, et al. Selenium@mesoporous carbon composite with superior lithium and sodium storage capacity. *ACS Nano*. 2013;7(9):8003-8010.
27. Jian ZL, Luo W, Ji XL. Carbon electrodes for K-ion batteries. *J Am Chem Soc*. 2015;137(36):11566-11569.
28. Han J, Niu YB, Bao SJ, Yu YN, Lu SY, Xu MW. Nanocubic $KTi_2(PO_4)_3$ electrodes for potassium-ion batteries. *Chem Commun*. 2016;52(78):11661-11664.
29. Pramudita JC, Sehrawat D, Goonetilleke D, Sharma N. An initial review of the status of electrode materials for potassium-ion batteries. *Adv Energy Mater*. 2017;7(24):1602911.
30. Muldoon J, Bucur CB, Oliver AG, et al. Electrolyte roadblocks to a magnesium rechargeable battery. *Energy Environ Sci*. 2012; 5(3):5941-5950.
31. Saha P, Datta MK, Velikokhatnyi OI, Manivannan A, Alman D, Kumta PN. Rechargeable magnesium battery: current status and key challenges for the future. *Prog Mater Sci*. 2014;66:1-86.
32. Nam KW, Kim S, Lee S, et al. The high performance of crystal water containing manganese birnessite cathodes for magnesium batteries. *Nano Lett*. 2015;15(6):4071-4079.
33. Ponrouch A, Frontera C, Barde F, Palacin MR. Towards a calcium-based rechargeable battery. *Nat Mater*. 2016;15(2): 169-173.
34. Chen X, Zhong C, Liu B, et al. Atomic layer Co_3O_4 nanosheets: the key to knittable Zn-air batteries. *Small*. 2018;14(43): 1702987.
35. Chen X, Liu B, Zhong C, et al. Ultrathin Co_3O_4 layers with large contact area on carbon fibers as high-performance electrode for flexible zinc-air battery integrated with flexible display. *Adv Energy Mater*. 2017;7(18):1700779.
36. Kundu D, Adams BD, Duffort V, Vajargah SH, Nazar LF. A high-capacity and long-life aqueous rechargeable zinc battery using a metal oxide intercalation cathode. *Nat Energy*. 2016;1: 16119.
37. Yan MY, He P, Chen Y, et al. Water-lubricated intercalation in $V_2O_5{\cdot}nH_2O$ for high-capacity and high-rate aqueous rechargeable zinc batteries. *Adv Mater*. 2018;30(1):1703725.
38. Zhang XL, Tang YB, Zhang F, Lee CS. A novel aluminum-graphite dual-ion battery. *Adv Energy Mater*. 2016;6(11): 1502588.
39. Zhang M, Song XH, Ou XW, Tang YB. Rechargeable batteries based on anion intercalation graphite cathodes. *Energy Storage Mater*. 2019;16:65-84.
40. Chen H, Guo F, Liu YJ, et al. A defect-free principle for advanced graphene cathode of aluminum-ion battery. *Adv Mater*. 2017;29(12):1605958.
41. Li HC, Yang HC, Sun ZH, Shi Y, Cheng HM, Li F. A highly reversible Co_3S_4 microsphere cathode material for aluminum-ion batteries. *Nano Energy*. 2019;56:100-108.
42. Choi JW, Aurbach D. Promise and reality of post-lithiumion batteries with high energy densities. *Nat Rev Mater*. 2016;1:16013.
43. Speirs J, Contestabile M, Houari Y, Gross R. The future of lithium availability for electric vehicle batteries. *Renew Sust Energ Rev*. 2014;35:183-193.
44. Olivetti EA, Ceder G, Gaustad GG, Fu X. Lithium-ion battery supply chain considerations: analysis of potential bottlenecks in critical metals. *Joule*. 2017;1(2):229-243.
45. Yan J, Wang J, Liu H, Bakenov Z, Gosselink D, Chen P. Rechargeable hybrid aqueous batteries. *J Power Sources*. 2012; 216:222-226.
46. Alias N, Mohamad AA. Advances of aqueous rechargeable lithium-ion battery: a review. *J Power Sources*. 2015;274: 237-251.

47. Kim H, Hong J, Park KY, Kim H, Kim SW, Kang K. Aqueous rechargeable Li and Na ion batteries. *Chem Rev*. 2014;114(23): 11788-11827.
48. Suo LM, Borodin O, Sun W, et al. Advanced high-voltage aqueous lithium-ion battery enabled by "water-in-Bisalt" electrolyte. *Angew Chem Int Ed*. 2016;55(25):7136-7141.
49. Wang LP, Wang PF, Wang TS, Yin YX, Guo YG, Wang CR. Prussian blue nanocubes as cathode materials for aqueous Na-Zn hybrid batteries. *J Power Sources*. 2017;355:18-22.
50. Su DW, Andrew MD, Qiao SZ, Wang GX. High-capacity aqueous potassium-ion batteries for large-scale energy storage. *Adv Mater*. 2017;29(1):1604007.
51. Liu S, Hu JJ, Yan NF, Pan GL, Li GR, Gao XP. Aluminum storage behavior of anatase TiO_2 nanotube arrays in aqueous solution for aluminum ion batteries. *Energy Environ Sci*. 2012;5(12): 9743-9746.
52. Luo JY, Cui WJ, He P, Xia YY. Raising the cycling stability of aqueous lithium-ion batteries by eliminating oxygen in the electrolyte. *Nat Chem*. 2010;2:760-765.
53. Ming J, Guo J, Xia C, Wang WX, Alshareef HN. Zinc-ion batteries: materials, mechanisms, and applications. *Mater Sci Eng R*. 2019;135:58-84.
54. Song M, Tan H, Chao DL, Fan HJ. Recent advances in Zn-ion batteries. *Adv Funct Mater*. 2018;28(41):1802564.
55. Fang GZ, Zhou J, Pan AQ, Liang SQ. Recent advances in aqueous zinc-ion batteries. *ACS Energy Lett*. 2018;3(10):2480-2501.
56. Zeng XH, Hao JN, Wang ZJ, Mao JF, Guo ZP. Recent progress and perspectives on aqueous Zn-based rechargeable batteries with mild aqueous electrolytes. *Energy Storage Mater*. 2019;20: 410-437.
57. Yu P, Zeng YX, Zhang HZ, Yu MH, Tong YX, Lu XH. Flexible Zn-ion batteries: recent progresses and challenges. *Small*. 2019; 15(7):1804760.
58. Wan F, Niu Z. Design strategies of vanadium-based aqueous zinc-ion batteries. *Angew Chem Int Ed* In press. https://doi.org/10.1002/anie.201903941.
59. Zhang N, Dong Y, Jia M, et al. Rechargeable aqueous Zn-V_2O_5 battery with high energy density and long cycle life. *ACS Energy Lett*. 2018;3(6):1366-1372.
60. Guo X, Fang GZ, Zhang WY, et al. Mechanistic insights of Zn^{2+} storage in sodium vanadates. *Adv Energy Mater*. 2018;8(27): 1801819.
61. Islam S, Alfaruqi MH, Mathew V, et al. Facile synthesis and the exploration of the zinc storage mechanism of β-MnO_2 nanorods with exposed (101) planes as a novel cathode material for high performance eco-friendly zinc-ion batteries. *J Mater Chem A*. 2017;5(44):23299-23309.
62. Zhang N, Cheng FY, Liu JX, et al. Rechargeable aqueous zinc-manganese dioxide batteries with high energy and power densities. *Nat Commun*. 2017;8:405.
63. Wan F, Zhang LL, Dai X, Wang XY, Niu ZQ, Chen J. Aqueous rechargeable zinc/sodium vanadate batteries with enhanced performance from simultaneous insertion of dual carriers. *Nat Commun*. 2018;9:1656.
64. Alfaruqi MH, Gim J, Kim S, et al. Enhanced reversible divalent zinc storage in a structurally stable α-MnO_2 nanorod electrode. *J Power Sources*. 2015;288:320-327.
65. He P, Yan MY, Zhang GB, et al. Layered VS_2 nanosheet-based aqueous Zn ion battery cathode. *Adv Energy Mater*. 2017;7(11): 1601920.
66. Li GL, Yang Z, Jiang Y, et al. Towards polyvalent ion batteries: a zinc-ion battery based on NASICON structured $Na_3V_2(PO_4)_3$. *Nano Energy*. 2016;25:211-217.
67. Alfaruqi MH, Mathew V, Song J, et al. Electrochemical zinc intercalation in lithium vanadium oxide: a high-capacity zinc-ion battery cathode. *Chem Mater*. 2017;29(4):1684-1694.
68. Liu Z, Pulletikurthi G, Endres F. A Prussian blue/zinc secondary battery with a bio-ionic liquid-water mixture as electrolyte. *ACS Appl Mater Interfaces*. 2016;8(19):12158-12164.
69. Trócoli R, Mantia FL. An aqueous zinc-ion battery based on copper hexacyanoferrate. *ChemSusChem*. 2015;8(3):481-485.
70. Zhang LY, Chen L, Zhou XF, Liu ZP. Towards high-voltage aqueous metal-ion batteries beyond 1.5 V: the zinc/zinc hexacyanoferrate system. *Adv Energy Mater*. 2015;5(2):1400930.
71. Trocoli R, Kasiri G, Mantia FL. Phase transformation of copper hexacyanoferrate ($KCuFe[CN]_6$) during zinc insertion: effect of co-ion intercalation. *J Power Sources*. 2018;400:167-171.
72. Post JE. Manganese oxide minerals: crystal structures and economic and environmental significance. *Proc Natl Acad Sci*. 1999; 96(7):3447-3454.
73. Wei WF, Cui XW, Chen WX, Ivey DG. Manganese oxide-based materials as electrochemical supercapacitor electrodes. *Chem Soc Rev*. 2011;40:1697-1721.
74. Juran TR, Young J, Smeu M. Density functional theory modeling of MnO_2 polymorphs as cathodes for multivalent ion batteries. *J Phys Chem C*. 2018;122(16):8788-8795.
75. Cheng FY, Chen J, Gou XL, Shen PW. High-power alkaline Zn-MnO_2 batteries using γ-MnO_2 nanowires/nanotubes and electrolytic zinc powder. *Adv Mater*. 2005;17(22):2753-2756.
76. Liu HW, Liu JY, Yang Z, Tang DG. Controlled construction of hierarchical hollow micro/nano urchin-like β-MnO_2 with superior lithium storage performance. *J Alloys Compd*. 2019;795: 336-342.
77. Voskanyan AA, Ho CK, Chan KY. 3D δ-MnO_2 nanostructure with ultralarge mesopores as high-performance lithium-ion battery anode fabricated via colloidal solution combustion synthesis. *J Power Sources*. 2019;421:162-168.
78. Li H, Liu A, Zhao S, Guo ZL, Wang NN, Ma TL. In situ growth of a feather-like MnO_2 nanostructure on carbon paper for high-performance rechargeable sodium-ion batteries. *Chem Electro Chem*. 2018;5:3266-3272.
79. Chong SK, Wu YF, Liu CF, et al. Cryptomelane-type MnO_2/carbon nanotube hybrids as bifunctional electrode material for high capacity potassium-ion full batteries. *Nano Energy*. 2018;54:106-115.
80. Liu ZX, Pang G, Dong SY, Zhang YD, Mi CH, Zhang XG. An aqueous rechargeable sodium-magnesium mixed ion battery based on $NaTi_2(PO_4)_3$-MnO_2 system. *Electrochim Acta*. 2019; 311:1-7.
81. Tekin B, Cakan RD. Understanding the role of water-based electrolytes on magnesium-ion insertion/extraction into λ-MnO_2 lattice structure. *Solid State Ionics*. 2019;335:67-73.
82. Mao ML, Gao T, Hou S, Wang CS. A critical review of cathodes for rechargeable mg batteries. *Chem Soc Rev*. 2018;47(23):8804-8841.

83. Han SD, Soojeong Kim S, Li DG, et al. Mechanism of Zn insertion into nanostructured δ-MnO_2: a nonaqueous rechargeable Zn metal battery. *Chem Mater*. 2017;29(11):4874-4884.
84. Zhao S, Han B, Zhang DT, et al. Unravelling the reaction chemistry and degradation mechanism in aqueous Zn/MnO_2 rechargeable batteries. *J Mater Chem A*. 2018;6(14):5733-5739.
85. Alfaruqi MH, Islam S, Gim J, et al. A high surface area tunnel-type α-MnO_2 nanorod cathode by a simple solvent-free synthesis for rechargeable aqueous zinc-ion batteries. *Chem Phys Lett*. 2016;650:64-68.
86. Liu Q, Hao ZM, Liao XB, et al. Langmuir–Blodgett nanowire devices for in situ probing of zinc-ion batteries. *Small*. 2019;15(30):1902141.
87. Su DW, Ahn HJ, Wang GX. Hydrothermal synthesis of α-MnO_2 and β-MnO_2 nanorods as high capacity cathode materials for sodium ion batteries. *J Mater Chem A*. 2013;1(11):4845-4850.
88. Luo JY, Zhang JJ, Xia YY. Highly electrochemical reaction of lithium in the ordered mesoporosus β-MnO_2. *Chem Mater*. 2006;18(23):5618-5623.
89. Chen WM, Qie L, Shao QG, Yuan LX, Zhang WX, Huang YH. Controllable synthesis of hollow bipyramid β-MnO_2 and its high electrochemical performance for lithium storage. *ACS Appl Mater Interfaces*. 2012;4(6):3047-3053.
90. Xu CJ, Li BH, Du HD, Kang FY. Energetic zinc ion chemistry: the rechargeable zinc ion battery. *Angew Chem Int Ed*. 2012;51(4):933-935.
91. Wei CG, Xu CJ, Li BH, Du HD, Kang FY. Preparation and characterization of manganese dioxides with nano-sized tunnel structures for zinc ion storage. *J Phys Chem Solids*. 2012;73(12):1487-1491.
92. Devaraj S, Munichandraiah N. Effect of crystallographic structure of MnO_2 on its electrochemical capacitance properties. *J Phys Chem C*. 2008;112(11):4406-4417.
93. Luo JY, Xia YY. Effect of pore structure on the electrochemical capacitive performance of MnO_2. *J Electrochem Soc*. 2007;154(11):A987-A992.
94. Yamamoto T, Shoji T. Rechargeable Zn $|ZnSO_4|MnO_2$-cells. *Inorg Chim Acta*. 1986;117:L27-L28.
95. Kumar GG, Sampath S. Electrochemical characterization of poly (vinylidenefluoride)-zinc triflate gel polymer electrolyte and its application in solid-state zinc batteries. *Solid State Ionics*. 2003;160(3–4):289-300.
96. Alfaruqi MH, Mathew V, Gim J, et al. Electrochemically induced structural transformation in a γ-MnO_2 cathode of a high capacity zinc-ion battery system. *Chem Mater*. 2015;27(10):3609-3620.
97. Feng Q, Yanagisawa K, Yamasaki N. Hydrothermal soft chemical process for synthesis of manganese oxides with tunnel structures. *J Porous Mater*. 1998;5(2):153-161.
98. Xu CJ, Du HD, Li BH, Kang FY, Zeng YQ. Reversible insertion properties of zinc ion into manganese dioxide and its application for energy storage. *Electrochem Solid-State Lett*. 2009;12(4):A61-A65.
99. Lee B, Yoon CS, Lee HR, Chung KY, Cho BW, Oh SH. Electrochemically induced reversible transition from the tunneled to layered polymorphs of manganese dioxide. *Sci Rep*. 2014;4:6066.
100. Lee B, Lee HR, Kim H, Chung KY, Cho BW, Oh SH. Elucidating the intercalation mechanism of zinc ions into α-MnO_2 for rechargeable zinc batteries. *Chem Commun*. 2015;51(45):9265-9268.
101. Lee B, Seo HR, Lee HR, et al. Critical role of pH evolution of electrolyte in the reaction mechanism for rechargeable zinc batteries. *ChemSusChem*. 2016;9(20):2948-2956.
102. Pan H, Shao Y, Yan P, et al. Reversible aqueous zinc/mangane storage from conversion reactions. *Nat Energy*. 2016;1:16039.
103. Fang GZ, Zhu CY, Chen MH, et al. Suppressing manganese dissolution in potassium manganate with rich oxygen defects engaged high-energy-density and durable aqueous zinc-ion battery. *Adv Funct Mater*. 2019;29(15):1808375.
104. Feng Q, Kanoh H, Miyai Y, Ooi K. Metal ion extraction/insertion reactions with todorokite-type manganese oxide in the aqueous phase. *Chem Mater*. 1995;7:1722-1727.
105. Golden DC, Chen CC, Dixon JB. Transformation of birnessite to buserite, todorokite, and manganite under mild hydrothermal treatment. *Clay Clay Miner*. 1987;35(4):271-280.
106. Sun ZJ, Chen HY, Shu D, He C, Tang SQ, Zhang J. Supercapacitive behavior and high cycle stability of todorokite-type manganese oxide with large tunnels. *J Power Sources*. 2012;203:233-242.
107. Post JE, Bish DL. Rietveld refinement of the todorokite structure. *Am Mineral*. 1988;73(7–8):861-869.
108. Lee J, Ju JB, Cho WI, Cho BW, Oh SH. Todorokite-type MnO_2 as a zinc-ion intercalating material. *Electrochim Acta*. 2013;112:138-143.
109. Simon DE, Morton RW, Gislason JJ. A close look at electrolytic manganese dioxide (EMD) and the γ-MnO_2 & ε-MnO_2 phases using rietveld modeling. *Adv X-ray Anal*. 2004;47:267-280.
110. Sun W, Wang F, Hou S, et al. Zn/MnO_2 battery chemistry with H^+ and Zn^{2+} Coinsertion. *J Am Chem Soc*. 2017;139(29):9775-9778.
111. Chao DL, Zhou WH, Ye C, et al. An electrolytic Zn-MnO_2 battery demonstrated for high-voltage and scalable energy storage. *Angew Chem Int Ed*. 2019;58(23):7823-7828.
112. Alfaruqi MH, Gim J, Kim S, et al. A layered δ-MnO_2 nanoflake cathode with high zinc-storage capacities for eco-friendly battery applications. *Electrochem Commun*. 2015;60:121-125.
113. Huang J, Wang Z, Hou M, et al. Polyaniline-intercalated manganese dioxide nanolayers as a high-performance cathode material for an aqueous zinc-ion battery. *Nat Commun*. 2018;9:2906.
114. Du GD, Wang JQ, Guo ZP, Chen ZX, Liu HK. Layered δ-MnO_2 as positive electrode for lithium intercalation. *Mater Lett*. 2011;65(9):1319-1322.
115. Liu Y, Qiao Y, Zhang WX, et al. Nanostructured alkali cation incorporated δ-MnO_2 cathode materials for aqueous sodium-ion batteries. *J Mater Chem A*. 2015;3(15):7780-7785.
116. Alfaruqi MH, Islam S, Putro DY, et al. Structural transformation and electrochemical study of layered MnO_2 in rechargeable aqueous zinc-ion battery. *Electrochim Acta*. 2018;276:1-11.
117. Jiang BZ, Xu CJ, Wu CL, Dong LB, Li J, Kang FY. Manganese sesquioxide as cathode material for multivalent zinc ion battery with high capacity and long cycle life. *Electrochim Acta*. 2017;229:422-428.
118. Nolis GM, Adil A, Yoo HD, et al. Electrochemical reduction of a spinel-type manganese oxide cathode in aqueous electrolytes with Ca^{2+} or Zn^{2+}. *J Phys Chem C*. 2018;122(8):4182-4188.
119. Hao JW, Mou J, Zhang JW, et al. Electrochemically induced spinel-layered phase transition of Mn_3O_4 in high performance neutral aqueous rechargeable zinc battery. *Electrochim Acta*. 2018;259:170-178.

120. Wu BK, Zhang GB, Yan MY, et al. Graphene scroll-coated α-MnO_2 nanowires as high performance cathode materials for aqueous Zn-ion battery. *Small*. 2018;14(13):1703850.
121. Nam KW, Kim H, Choi JH, Choi JW. Crystal water for high performance layered manganese oxide cathodes in aqueous rechargeable zinc batteries. *Energy Environ Sci*. 2019;12(6): 1999-2009.
122. Zhu CY, Fang GZ, Zhou J, et al. Binder-free stainless steel@Mn_3O_4 nanoflower composite: a high-activity aqueous zinc-ion battery cathode with high-capacity and long cycle-life. *J Mater Chem A*. 2018;6(20):9677-9683.
123. Wang YG, Li HQ, He P, Hosono E, Zhou HS. Nano active materials for lithium-ion batteries. *Nanoscale*. 2010;2(8):1294-1305.
124. Lee KT, Cho J. Roles of nanosize in lithium reactive nanomaterials for lithium ion batteries. *Nano Today*. 2011;6(1): 28-41.
125. Yu ZN, Tetard L, Zhai L, Thoma J. Supercapacitor electrode materials: nanostructures from 0 to 3 dimensions. *Energy Environ Sci*. 2015;8(3):702-730.
126. Gaberscek M, Dominko R, Jamnik J. Is small particle size more important than carbon coating? An example study on LiFePO4 cathodes. *Electrochem Commun*. 2007;9(12):2778-2783.
127. Ye SH, Lv JY, Gao XP, Wu F, Song DY. Synthesis and electrochemical properties of $LiMn_2O_4$ spinel phase with nanostructure. *Electrochim Acta*. 2004;49:1623-1628.
128. Yang JL, Hu L, Zheng JX, et al. Li_2FeSiO_4 nanorods bonded with graphene for high performance batteries. *J Mater Chem A*. 2015;3(18):9601-9608.
129. Song HQ, Liu YG, Zhang CP, Liu CF, Cao GZ. Mo-doped LiV_3O_8 nanorod-assembled nanosheets as a high performance cathode material for lithium ion batteries. *J Mater Chem A*. 2015; 3(7):3547-3558.
130. Cavaliere S, Subianto S, Savych I, Jones DJ, Rozière J. Electrospinning: designed architectures for energy conversion and storage devices. *Energy Environ Sci*. 2011;4(12):4761-4785.
131. Peng L, Fang ZW, Zhu Y, Yan CS, Yu GH. Holey 2D nanomaterials for electrochemical energy storage. *Adv Energy Mater*. 2018;8(9):1702179.
132. Liu JH, Liu XW. Two-dimensional nanoarchitectures for lithium storage. *Adv Mater*. 2012;24(20):4097-4111.
133. Chen RJ, Zhao TL, Zhang XX, Li L, Wu F. Advanced cathode materials for lithium-ion batteries using nanoarchitectonics. *Nanoscale Horiz*. 2016;1:423-444.
134. Cong L, Xie HM, Li JH. Hierarchical structures based on two-dimensional nanomaterials for rechargeable lithium batteries. *Adv Energy Mater*. 2017;7(12):1601906.
135. Xu M, Futaba DN, Yumura M, Hata K. Carbon nanotubes with temperature-invariant ceep and creep-recovery from −190 to 970 °C. *Adv Mater*. 2011;23(32):3686-3691.
136. Uetani K, Ata S, Tomonoh S, Yamada T, Yumura M, Hata K. Elastomeric thermal interface materials with high through-plane thermal conductivity from carbon fiber fillers vertically aligned by electrostatic flocking. *Adv Mater*. 2014;26(33):5857-5862.
137. Charlier JC, Blase X, Roche S. Electronic and transport properties of nanotubes. *Rev Mod Phys*. 2007;79(2):677-732.
138. Ni JF, Li Y. Carbon nanomaterials in different dimensions for electrochemical energy storage. *Adv Energy Mater*. 2016;6(17): 1600278.
139. Xu DW, Li BH, Wei CG, et al. Preparation and characterization of MnO_2/acid-treated CNT nanocomposites for energy storage with zinc ions. *Electrochim Acta*. 2014;133:254-261.
140. Xia J, Chen F, Li J, Tao N. Measurement of the quantum capacitance of graphene. *Nat Nanotechnol*. 2009;4:505-509.
141. Fang GZ, Zhou J, Liang CW, et al. MOFs nanosheets derived porous metal oxide-coated three-dimensional substrates for lithium-ion battery applications. *Nano Energy*. 2016;26:57-65.
142. Kong DZ, Luo JS, Wang YL, et al. Three-dimensional Co_3O_4@MnO_2 hierarchical nanoneedle arrays: morphology control and electrochemical energy storage. *Adv Funct Mater*. 2014; 24(24):3815-3826.
143. Chao DL, Xia XH, Liu JL, et al. A V_2O_5/conductive-polymer core/shell nanobelt array on three-dimensional graphite foam: a high-rate, ultrastable, and freestanding cathode for lithium-ion batteries. *Adv Mater*. 2014;26(33):5794-5800.
144. Liu SN, Wu J, Zhou J, Fang GZ, Liang SQ. Mesoporous $NiCo_2O_4$ nanoneedles grown on three dimensional graphene networks as binder-free electrode for high-performance lithium-ion batteries and supercapacitors. *Electrochim Acta*. 2015;176:1-9.
145. Khan MA, Erementchouk M, Hendrickson J, Leuenberger MN. Electronic and optical properties of vacancy defects in single-layer transition metal dichalcogenides. *Phys Rev B*. 2017;95(24): 245435.
146. Hu LP, Zhu TJ, Liu XH, Zhao XB. Point defect engineering of high-performance bismuth-telluride-based thermoelectric materials. *Adv Funct Mater*. 2014;24(33):5211-5218.
147. Lin Z, Carvalho BR, Kahn E, et al. Defect engineering of two-dimensional transition metal dichalcogenides. *2D Mater*. 2016;3: 022002.
148. Pan X, Yang MQ, Fu X, Zhang N, Xu YJ. Defective TiO_2 with oxygen vacancies: synthesis, properties and photocatalytic applications. *Nanoscale*. 2013;5(9):3601-3614.
149. Zhao Y, Chang C, Teng F, et al. Defect-engineered ultrathin δ-MnO_2 nanosheet arrays as bifunctional electrodes for efficient overall water splitting. *Adv Energy Mater*. 2017;7(18):1700005.
150. Kim HS, Cook JB, Lin H, et al. Oxygen vacancies enhance pseudocapacitive charge storage properties of MoO_{3-x}. *Nat Mater*. 2017;16:454-460.
151. Xiong T, Yu ZG, Wu HJ, et al. Defect engineering of oxygen-defcient manganese oxide to achieve high-performing aqueous zinc ion battery. *Adv Energy Mater*. 2019;9(14):1803815.
152. Wang RY, Shyam B, Stone KH, et al. Reversible multivalent (monovalent, divalent, trivalent) ion insertion in open framework materials. *Adv Energy Mater*. 2015;5(12):1401869.
153. Zhang N, Cheng FY, Liu YC, et al. Cation-deficient spinel $ZnMn_2O_4$ cathode in $Zn(CF_3SO_3)_2$ electrolyte for rechargeable aqueous Zn-ion battery. *J Am Chem Soc*. 2016;138(39):12894-12901.
154. Hu ZM, Xiao X, Huang L, et al. 2D vanadium doped manganese dioxides nanosheets for pseudocapacitive energy storage. *Nanoscale*. 2015;7(38):16094-16099.
155. Hashem AM, Abdel-Latif AM, Abuzeid HM, et al. Improvement of the electrochemical performance of nanosized α-MnO_2 used as cathode material for Li-batteries by Sn-doping. *J Alloys Compd*. 2011;509(40):9669-9674.
156. Liu Q, Wang S, Cheng H. High rate capabilities Fe-doped EMD electrodes for Li/MnO_2 primary battery. *Int J Electrochim Sci*. 2013;8(8):10540-10548.

157. Alfaruqi MH, Islam S, Mathew V, et al. Ambient redox synthesis of vanadium-doped manganese dioxide nanoparticles and their enhanced zinc storage properties. *Appl Surf Sci*. 2017;404:435-442.
158. He P, Zhang GB, Liao XB, et al. Sodium ion stabilized vanadium oxide nanowire cathode for high-performance zinc-ion batteries. *Adv Energy Mater*. 2018;8(10):702463.
159. Xia C, Guo J, Li P, Zhang XX, Alshareef NH. Highly stable aqueous zinc-ion storage using a layered calcium vanadium oxide bronze cathode. *Angew Chem Int Ed*. 2018;57(15):3943-3948.
160. Yang Y, Tang Y, Fang G, et al. Li^+ intercalated $V_2O_5{\cdot}nH_2O$ with enlarged layer spacing and fast ion diffusion as an aqueous zinc-ion battery cathode. *Energy Environ Sci*. 2018;11(11):3157-3162.
161. Qiu N, Chen H, Yang ZM, Sun S, Wang Y. Low-cost birnessite as a promising cathode for high-performance aqueous rechargeable batteries. *Electrochim Acta*. 2018;272:154-160.
162. Wang F, Borodin O, Gao T, et al. Highly reversible zinc metal anode for aqueous batteries. *Nat Mater*. 2018;17:543-549.
163. Liu QC, Xu JJ, Xu D, Zhang XB. Flexible lithium-oxygen battery based on a recoverable cathode. *Nat Commun*. 2015;6:7892.
164. Park J, Park M, Nam G, Lee J, Cho J. All-solid-state cable-type flexible zinc-air battery. *Adv Mater*. 2015;27(8):1396-1401.
165. Liu W, Song MS, Kong B, Cui Y. Flexible and stretchable energy storage: recent advances and future perspectives. *Adv Mater*. 2017;29(1):1603436.
166. Tan P, Chen B, Xu H, et al. Flexible Zn- and Li-air batteries: recent advances, challenges, and future perspectives. *Energy Environ Sci*. 2017;10(10):2056-2080.
167. Liu LL, Niu ZQ. Design and integration of flexible planar micro-supercapacitors. *Nano Res*. 2017;10(5):1524-1544.
168. Guo ZW, Zhao Y, YuxueDing YX, et al. Multi-functional flexible aqueous sodium-ion batteries with high safety. *Chem*. 2017;3(2):348-362.
169. Dong XL, Chen L, Su XL, Wang YG, Xia YY. Flexible aqueous lithium-ion battery with high safety and large volumetric energy density. *Angew Chem Int Ed*. 2016;55(26):7474-7477.
170. Yang CY, Ji X, Fan XL, et al. Flexible aqueous Li-ion battery with high energy and power densities. *Adv Mater*. 2017;29(44):1701972.
171. Huang Y, Liu JW, Huang QY, et al. Flexible high energy density zinc-ion batteries enabled by binder-free MnO_2/reduced graphene oxide electrode. *Npj Flexible Electron*. 2018;2:21.
172. Zeng YX, Zhang XY, Meng Y, et al. Achieving ultrahigh energy density and long durability in a flexible rechargeable quasi-solid-state Zn-MnO_2 battery. *Adv Mater*. 2017;29(26):1700274.
173. Li HF, Han CP, Huang Y, et al. An extremely safe and wearable solid-state zinc ion battery based on a hierarchical structured polymer electrolyte. *Energy Environ Sci*. 2018;11(4):941-951.
174. Zhang SL, Yu NS, Zeng S, et al. An adaptive and stable bio-electrolyte for rechargeable Zn-ion batteries. *J Mater Chem A*. 2018;6(26):12237-12243.
175. Mo FN, Liang GJ, Meng QQ, et al. A flexible rechargeable aqueous zinc manganese-dioxide battery working at −20 °C. *Energy Environ Sci*. 2019;12(2):706-715.
176. Wang ZF, Ruan ZH, Liu ZX, et al. A flexible rechargeable zinc-ion wire-shaped battery with shape memory function. *J Mater Chem A*. 2018;6(18):8549-8557.
177. Li HF, Liu ZX, Liang GJ, et al. Waterproof and tailorable elastic rechargeable yarn zinc ion batteries by a cross-linked polyacrylamide electrolyte. *ACS Nano*. 2018;12(4):3140-3148.

AUTHOR BIOGRAPHIES

Yinlei Zhao received his B.S. degree in Materials Science and Engineering from Jilin University in 2015. He is currently pursuing a Ph.D. under the supervision of Prof. Xin-;Bo Zhang at Changchun Institute of Applied Chemistry, Chinese Academy of Sciences. His current research interests include the design and synthesis of efficient energy storage materials and their application in ion batteries.

Yunhai Zhu received his B.S. degree in Materials Science and Engineering from Hubei University in 2014. He is currently pursuing a Ph.D. in Materials Science at Jilin University of China. His current interests include design and synthesis of functional materials for sodium-/ potassium-ion batteries and flexible energy storage device.

Xinbo Zhang is a Full Professor at Changchun Institute of Applied Chemistry (CIAC), Chinese Academy of Sciences (CAS). He obtained his Ph.D. in Inorganic Chemistry from CIAC and was granted the CAS Presidential Scholarship Award in 2005. From 2005–2009, he worked as a Japan Society for the Promotion of Science (JSPS) postdoctoral fellow (2005–2007) and a New Energy and Industrial Technology Development Organization (NEDO) research associate (2007–2009) at National Institute of Advanced Industrial Science and Technology (AIST), Japan. His interests mainly focus on functional inorganic materials for batteries, fuel cells and electrochemical catalysis.

How to cite this article: Zhao Y, Zhu Y, Zhang X. Challenges and perspectives for manganese-based oxides for advanced aqueous zinc-ion batteries. *InfoMat*. 2020;2:237–260. https://doi.org/10.1002/inf2.12042